MECH 498: Interdisciplinary Design Project I

Design of an Anti-Tilting Outdoor Mobile Robot

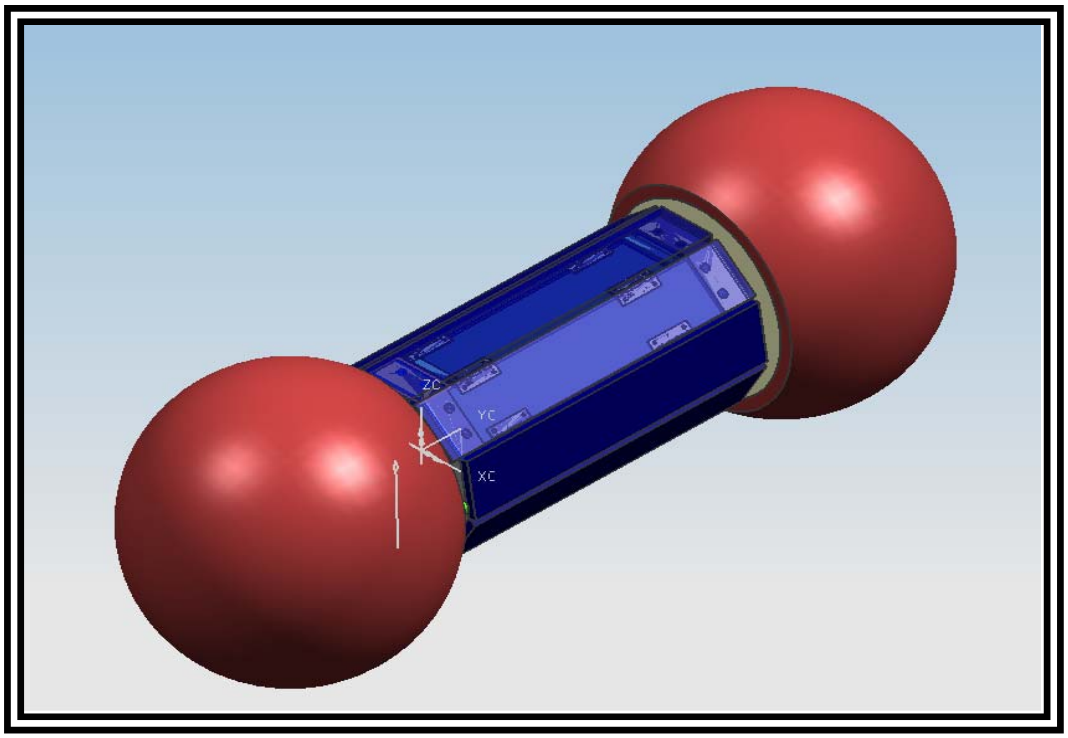

Submitted by: Sarah Stumpf, 260049266
Submitted to: Professor Jorge Angeles; Professor Timothy Lee

December 6th, 2006

Acknowledgements

I wish to express my sincere thanks to Professor Jorge Angeles for his guidance, advice, and suggestions over the course of the project. I would also like to thank Danielle Nasrallah, whose Ph. D. Thesis work was the inspiration for the entire design, and Phillipe Cardou, who helped me select instrumentation despite my little knowledge on the subject.

Contents

1.0 - Introduction

The work here presented is the current status and work done thus far on the design of an Anti-Tilting Outdoor Mobile (ATOM) robot, based on (Nasrallah, 2006). ATOM will be meant for outdoor navigation on uneven terrain, either on Earth or elsewhere (for example, Mars). Applications of such a robot include planetary exploration and mapping, as well as earth missions on terrain inaccessible to or dangerous for humans.

ATOM is to have two spherical wheels with a balancing central body, as depicted in *Figure 1*. The idea behind the wheel design is to avoid wheel slippage that can result in power loss and control system feedback errors (e.g. position sensor inaccuracies). The design also gives the robot the ability to continue its mission if flipped.

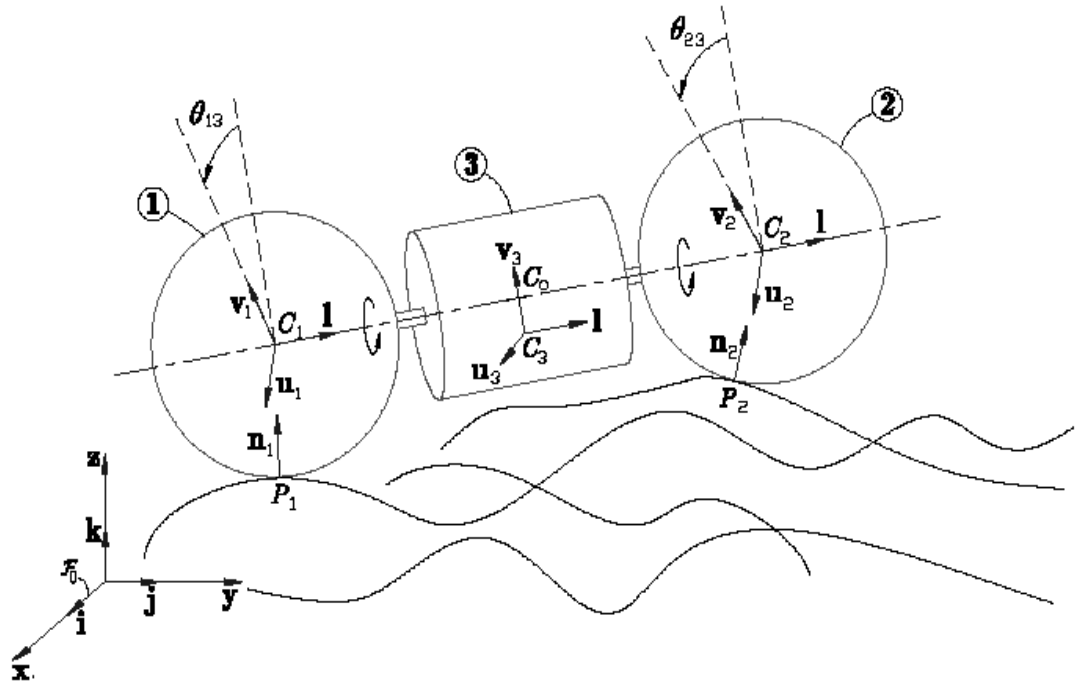

1

Figure 1: Conceptual Schematic of ATOM (Nasrallah, 2006)

The main design goals achieved at this stage are:

- A custom wheel and suspension system
- The coupling of the wheels to the central body
- A solar panel deployment/retraction mechanism
- The central body structure
- Impact force modeling

The components of ATOM are each being designed for the temperatures, solar intensity, dust, and gravity in the worst expected environment out of Mars and Earth. Substantial research was required regarding the Mars environment, driving on uneven terrain, impact force modeling, and photovoltaic systems, among other subjects.

Because there were a large number of variables to play with when determining the geometric, torque, force, motion, and power parameters, the analytical relationships were set up using *Maple* code. This allowed the numerical values of the required parameters to be easily varied during the iterative phase of the design without tedious hand repetitions of the calculations. The code can also be used for future optimization of the design. Although the script itself is not included in the report, the non-obvious equations, assumptions, and reasoning used are presented in the appropriate sections.

The impact model created for the system was analysed using *MATLAB* instead of *Maple*, due to its simulation capabilities. Both the *MATLAB* and *Maple* code have been retained for use in future phases of the ATOM design.

The major issues to be addressed during the next phase of the design are:

- Detailed design of the transmission system or equivalent mechanism (including motor choice)
- Detailed electrical load analysis and circuit design
- Computer programming

Other minor design aspects to be completed are presented throughout the report and summarized in the conclusion.

2.0 - Design Overview

2.1 - Strawman Task

The actual use of ATOM could be for a variety of tasks. For the design of the prototype, a Strawman task was thus defined as the topographical surveying of unknown terrain. The mission is intended to take place on Mars, and the prototype is designed to be tested at the Canadian Space Agency's Mars simulation site in Longueuil, QC. This test site is depicted in *Figure 2*.

Figure 2 (a): Smooth side of test site

Figure 2(b): Rocky side of test site

Based on the test terrain, ATOM will be designed to climb a maximum slope of 45

degrees. The simulation site is outdoors on Earth, and thus does not emulate the Martian climate; nevertheless, an attempt is made to design ATOM for the Martian irradiation, temperature, and ground texture. The following data were obtained about the Martian environment.

2.1.1 - Atmosphere

Martian day (Sol) duration:	24.66 hours
Temperature range:	140 to 350 K
Wind speeds:	3 to 7 m/s
Gravitational acceleration:	3.72 m/s^2

Mars irradiation data from landing sites of the spacecrafts *Viking 1* and *Viking 2* are displayed in *Figure 4*.

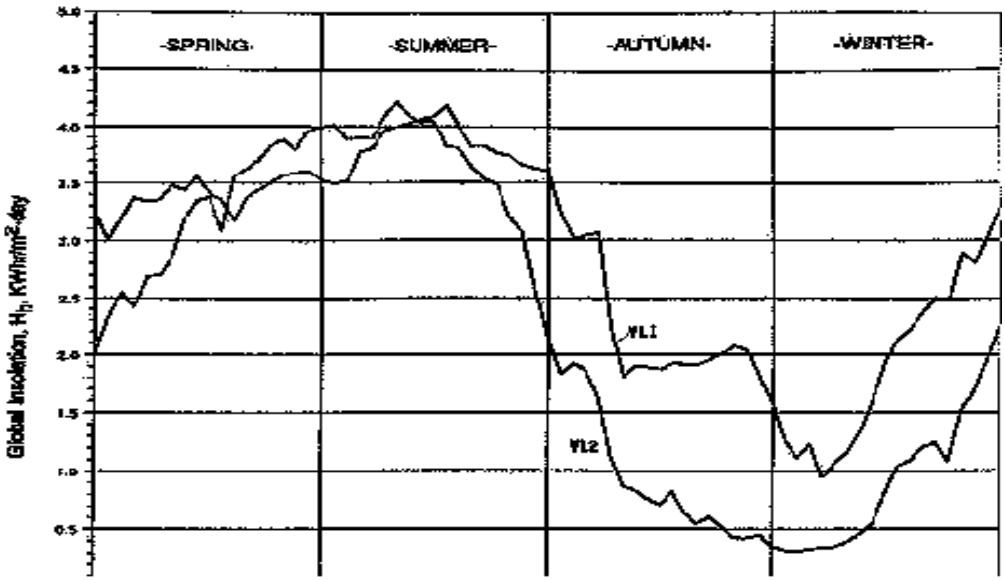

Figure 4: Insolation by season at Viking lander sites (Landis, 1991)

The mission is assumed near the equator, for which the plot of *Figure 5* shows hours of

daylight that are applicable.

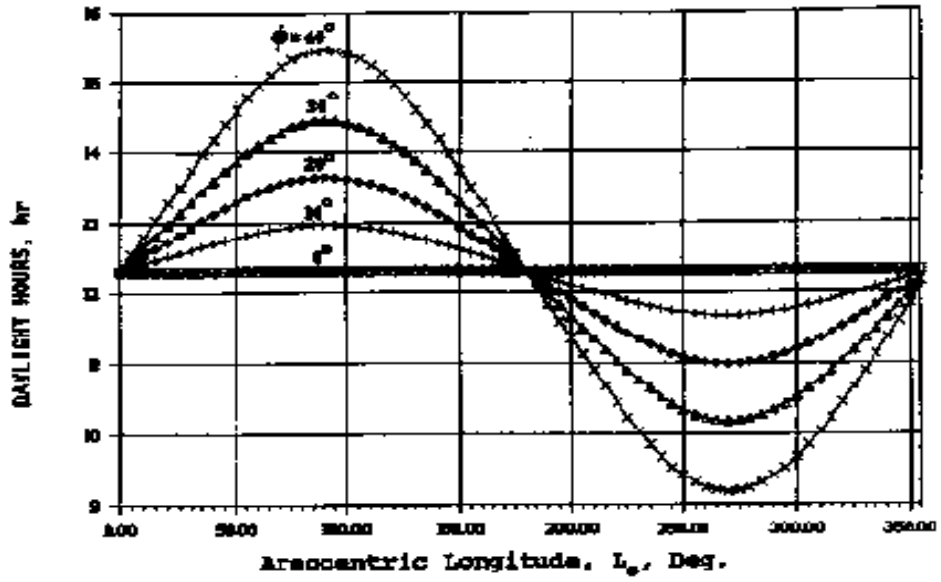

*Figure 5: Hours of daylight vs. Longitude (Landis, 1991)*2.1.2 – Terrain

Data pertaining to the Martian terrain are displayed in *Table 1*.

	Bearing strength	**Cohesion**	**Internal friction angle**	**Bulk density (soil)**	**Thermal inertia (soil)**
Gusev loose soils	5 kPa	1 kPa	20°	1230 kg/m^3 *)	134 J m^{-2} s$^{-1/2}$ K^{-1} **)
Gusev dense soils	200 kPa	15 kPa	25°	1483 kg/m^3 *)	153 J m^{-2} s$^{-1/2}$ K^{-1} **)
Meridiani Eagle crater floor & M. plains	80 kPa	5 kPa	20°	1333 kg/m^3 *)	142 J m^{-2} s$^{-1/2}$ K^{-1} **)
Meridiani Eagle crater wall (loose soil)	8 kPa	0.5 kPa	20°	1186 kg/m^3 *)	130 J m^{-2} s$^{-1/2}$ K^{-1} **)
VL-1 ‚drift'		1.6±1.2 kPa	18±2.4°	1150±150 kg/m^3	
VL-1 ‚blocky'		5.5±2.7 kPa	30.8±2.4°	1600±400 kg/m^3	
MPF ‚cloddy'		0.17±0.18 kPa	37.0±2.6°	1530±110 kg/m^3	

Table 1: Martian terrain data

2.2 - Design Description

What follows is a functional description of the major design components.

2.2.1 – Wheels

The ATOM wheel, depicted in *Figure 6*, is structured around a spherical metal *shell*, surrounded by a *rubber layer* meant to provide traction and disperse the impact force over a greater area of the shell than would be possible without a coating. The *wheel cylinder* acts as the wheel drive shaft, and is fixed to the shell by a *foam cushion*. The cushion fills all the empty wheel space with a shock absorbing foam, designed to protect the bearings and onboard equipment from potential impacts.

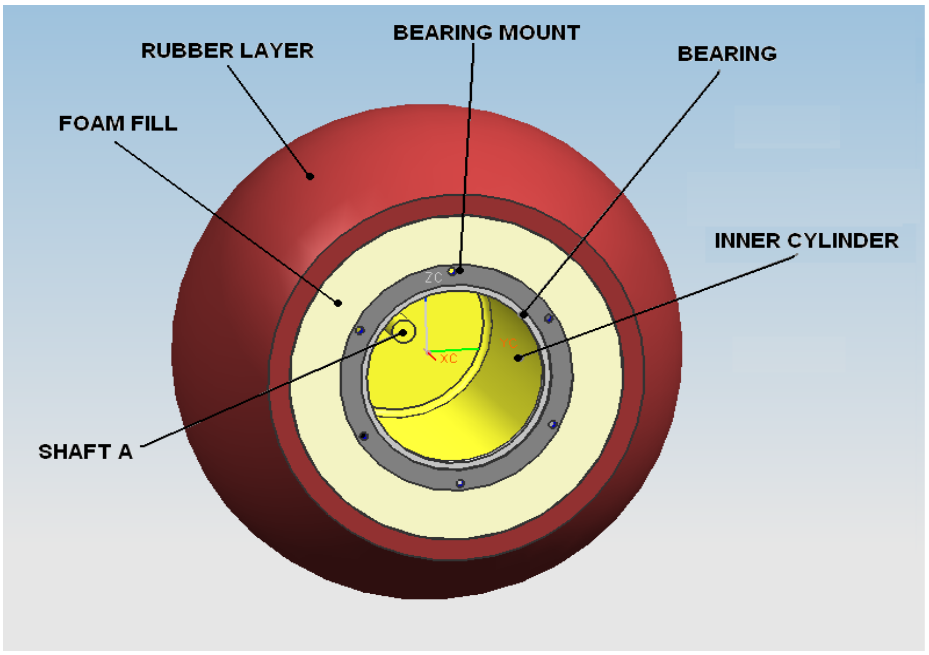

Figure 6: Wheel structure

2.2.2 – Wheel to Central Body Coupling

The wheel cylinder is mounted to the concentric *end cylinder* of the central body, shown in *Figure 7*, through a thin section *bearing*, allowing rotation of the wheel relative to the central body. The *drive shaft connection*, denoted **Shaft A**, is fixed to the wheel cylinder. A *transmission system* fixed to the central body (to be housed in the end cylinder) will be responsible for transmitting power from an *electric motor* to **Shaft A**, driving the wheel. The transmission system has yet to be designed, and a different transmission design will be needed for each wheel. The precise requirements of the transmission system are outlined later on.

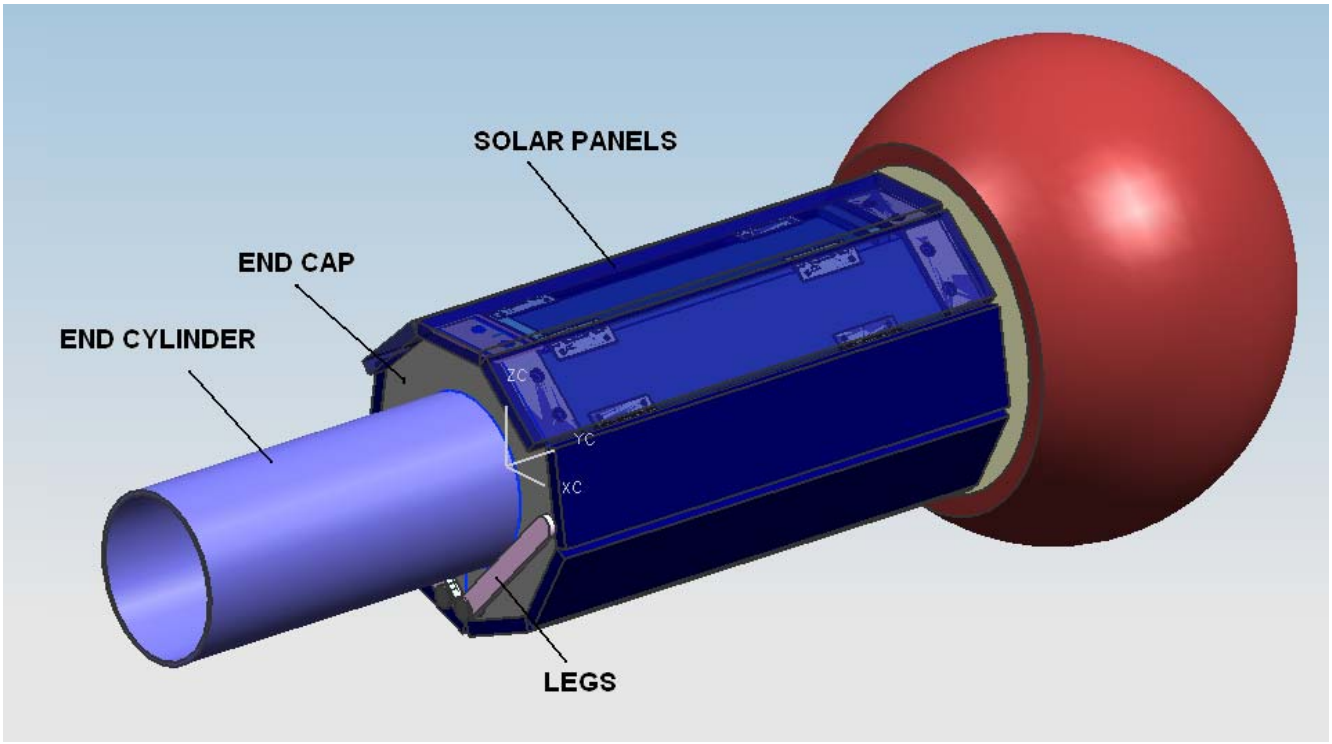

Figure 7: Drive mode with invisible wheel

2.2.3 – Central Body Structure

The end cylinders are connected to the *central body frame* by *end caps*. The end caps act as supports for the solar panels when in drive mode. They also create a clearance between the central body frame and solar panels, which allows space for heads of bolts (used to connect parts to the inside of the central body) and to channel solar panel wiring. The central body frame is actually composed of two pieces, as seen in *Figure 9*, to allow easy access to the components inside. The top piece is directly connected to the *central solar panel*. The central body frame is connected to the end caps by bolts, shown in *Figure 8*. Separating the central body frame from the wheels is simply a matter of removing the bolts and sliding off the end caps, making it easy to modify the inner layout. This also allows access to the components housed in the end cylinders.

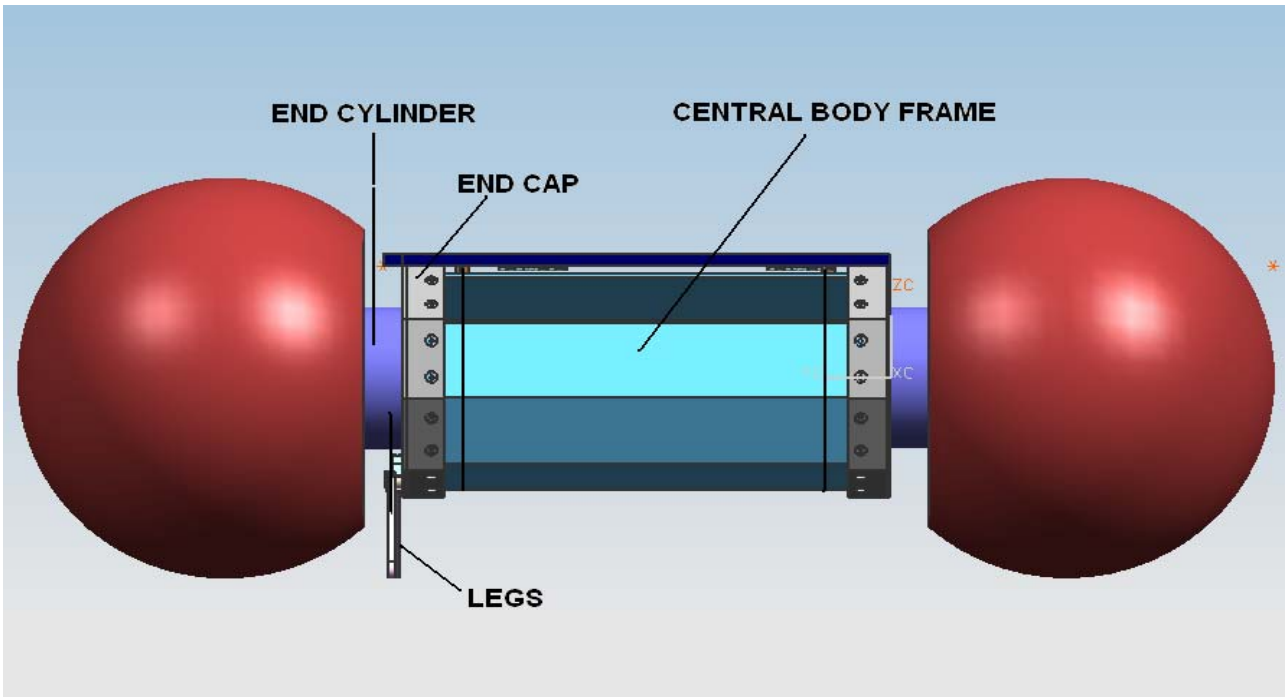

Figure 8: Front view with solar panels deployed

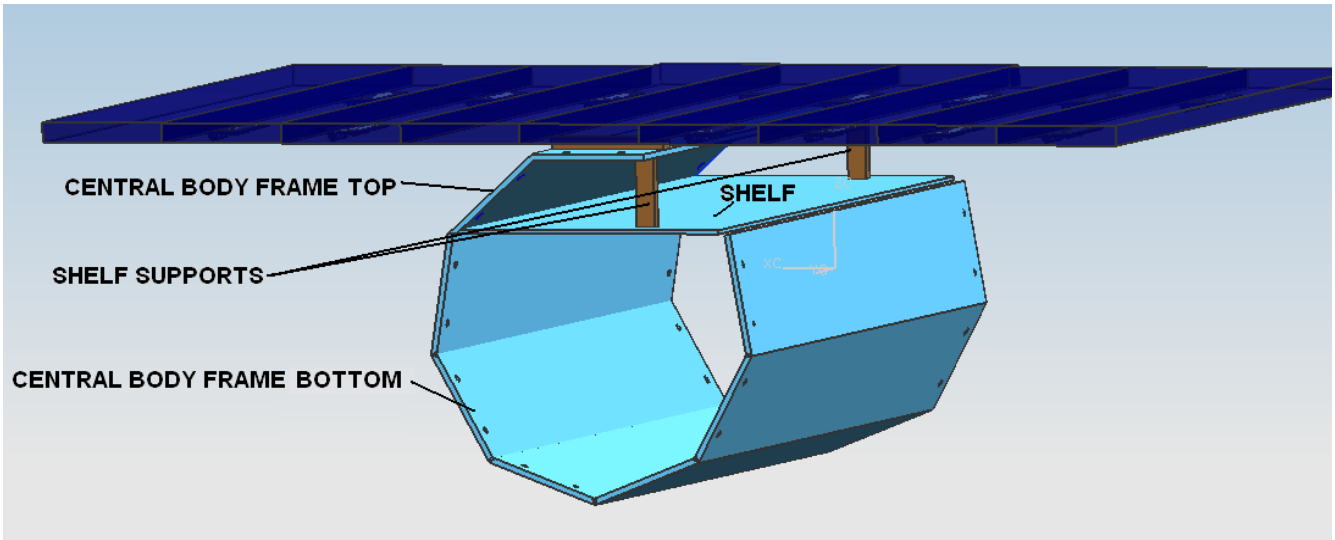

Figure 9: Stripped central body frame with solar panels deployed

2.2.4 – Solar Power System

ATOM will be powered by solar energy from an array of *solar panels* completely surrounding the central body, as shown in *Figure 7*. The robot is capable of going into charge mode, as depicted in *Figure 10*, to maximize solar energy captured. In this mode, *legs* are extended to keep the central body stable, and the solar panels unwrap from the central body to form a flat surface.

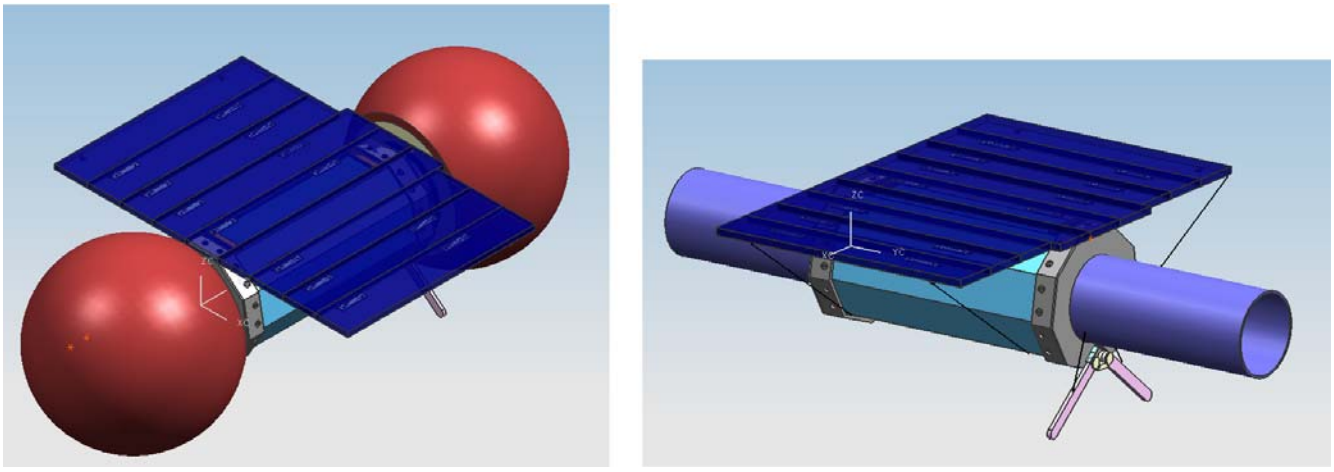

(a) *(b)*

Figure 10: Charge mode (a) full view (b) invisible wheels

Torsional hinges on the axis of rotation of the legs cause the legs to spring into their charge mode position when not restrained. Similarly, torsional hinges connecting the solar panels cause them to extend into the horizontal charge mode position when unrestrained. Note that a *leg break,* labeled in *Figure 11(a),* is present to prevent the legs from over-rotation which could result in instability.

The *panel cables* (**C Cables**) are connected at one end to the solar panels and at the other to the *panel winch* (**Winch C**) on **Shaft C**. A clockwise rotation of **Shaft C**, in reference to *Figure 11(a)*, causes the **C Cables** to wind around **Winch C**, forcing the solar panels to return to their drive (retracted) position. **Shaft C** can then be locked in place.

Similarly, a clockwise rotation of **Shaft B**, in reference to *Figure 11(a)*, causes the *leg cables* (denoted **B Cables**) to wind around the *leg winch* (**Winch B**). This forces the legs to return to their drive position, after which **Shaft B** can be locked in place for drive mode.

The transmission system will be responsible for using the electric motor power to lock, unlock, and rotate shafts **A**, **B**, and **C** in relation to the central body. The specific tasks of the transmission system, which has not yet been designed in detail, are presented later in the report.

The solar energy captured will be used to charge a set of lithium-ion batteries contained in the central body. All electrical loads in the system will draw power from these batteries.

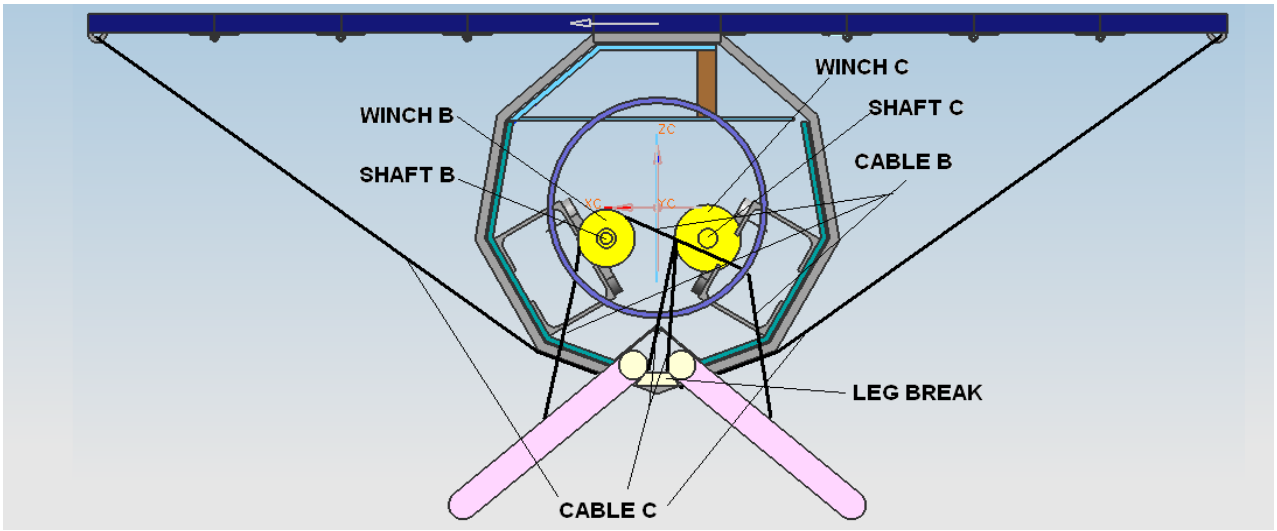

(a) all retraction mechanisms

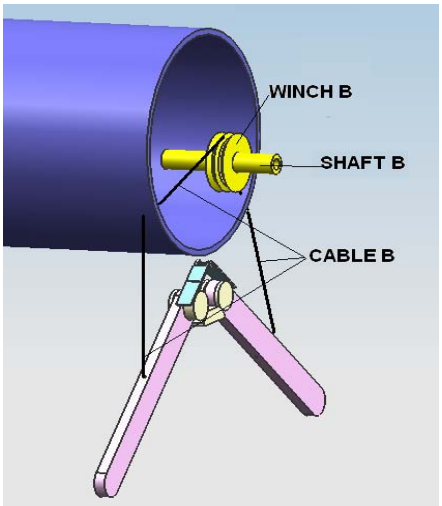

(b) retraction mechanism B

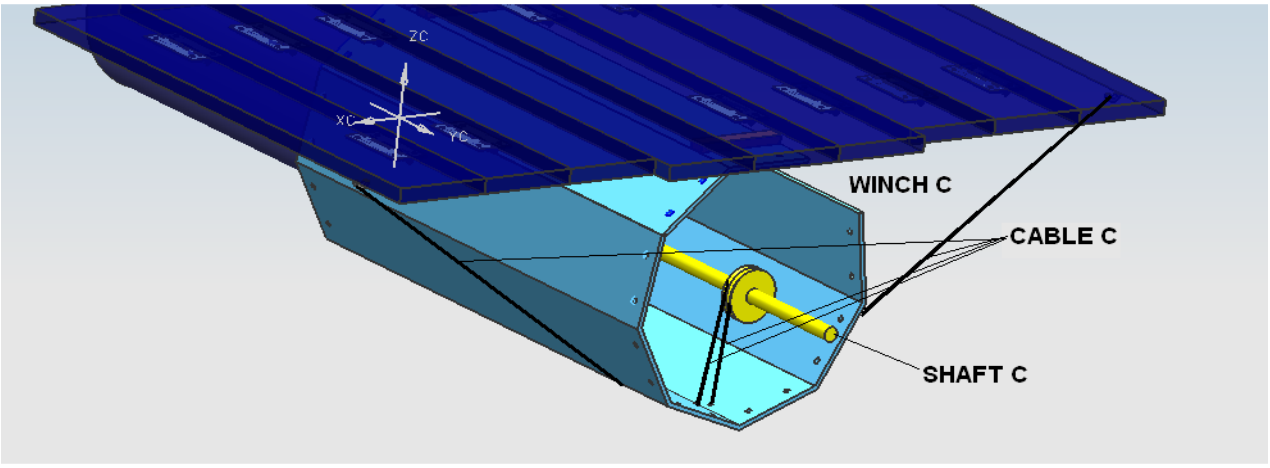

(c) retraction mechanism C

Figure 11: Simplified view of retraction mechanisms

2.2.5 - Instrumentation

The prototype design incorporates the *3DM-GX1® Gyro Enhanced Orientation Sensor* from *MicroStrain Inc.* to determine the pose, heading, speed, and location of ATOM based on a computer algorithm. A GPS unit may also be added if greater kinematic accuracy is required.

2.2.6 - Control and CPU

ATOM requires an internal transmitter and receiver for data transfer with the controller. A central processing unit will be located in the central body to communicate with the controller, transmission, motor, and sensors.

2.2.7 – Equipment Shelf

A shelf on which to store mission-specific equipment is included in the structure of the central body frame, as shown in *Figure 9.* When the solar panels are deployed, one side of the body frame polygon is open to the environment, allowing devices such as probes, robotic arms, and cameras to extend/gather information.

3.0 - Design Considerations

In this section, the components of the design are examined in detail. Some of the discarded concepts are presented along with reasons for the final component selections. The equations and assumptions employed are presented, as well as force and stress analysis.

3.1 - Wheels

It is essential to the ATOM design that the wheels be spherical in shape. Because this is a new concept for wheels, a custom design was required. Pneumatic wheels were first considered because they are excellent for impact absorption, but the shape requirement presented a rather challenging design problem that was beyond the scope of the project. It was thus decided to use a hollow spherical shell of metal, with a rubber layer to provide traction and reduce the impact on onboard equipment. Before this concept was developed, the rubber companies *Rematech Inc.* and *Elasto Proxy Inc*. were contacted about applying such a layer to confirm its feasibility.

The concept of ATOM requires a large wheel volume with respect to the central body. It was recognized early on that the large amount of empty space in the hollow wheels could in fact be used to house some of the robot components. The idea is to have the central body partially contained by the wheels. In addition to bettering space utilization, this concept provides a better load distribution as the weight will not be supported only at the edge of the wheel. With the wheels mounted in this manner, a type of suspension to absorb impact can also be included within the wheels.

3.1.1 - Structure

The spherical shell to be used for the wheel frame can be formed by a metal spinning process. A standard aluminum shell of outer diameter 12" (304.8 mm) and wall thickness 1/8" (3.175 mm) was selected. This product is available from *Franjo Metal Spinning Inc.* in 1100-0 aluminum, which has been used for the design. There are other manufacturers of such items that can be considered.

The density of aluminum 1100-0 is 2710kg/m^3, and the yield strength is Y_s = 24 - 34 MPa. Note that if greater strength were required for the shell, metals of up to 5/8" (15.9 mm) in thickness and perhaps greater could be spun by some companies (for example *Helander Metal Spinning Co.*). Another option is to replace the aluminum with steel.

3.1.2 – Rubber Layer

Through iteration, a thickness of t_R = 10 mm was selected for the rubber layer. It follows that the outer radius of the wheel is R_W = 162.4 mm.

Initially, it was desired to use the styrene-butadiene rubber (SBR) used for all season tires because of its proven performance in many types of vehicles. However, *Rematech Inc.*, who provided a quote for the application of the rubber layer, was unable to use SBR rubber because it does not have the rubber available in an uncured form. Neoprene rubber was thus selected because of its potential for the application as well as its abrasion-resistant properties. The density of the neoprene rubber is ρ_R = 1230 kg/m^3.

3.1.3 - Suspension

One of the main goals of the wheel design was to absorb the impact of a fall in order to protect the central body and its equipment. The impact experienced by the body can in theory be reduced to an arbitrary magnitude by increasing the thickness of the outer rubber accordingly. However, from a practical point of view this would add substantial weight to ATOM, since the rubber layer would need to cover the entire sphere. Because only a small area of the wheel will provide the impact "cushion", this is a rather inefficient method. It also presents problems from a manufacturing point of view.

More efficient ways of reducing impact were therefore examined. These involve shock absorption within the wheel that will account for impact in all three axes but accounting for less weight.

Pneumatic Tubes/Wheels

The idea here was to have pneumatic tubes or wheels within the spherical wheels, supporting the weight of the body. The advantage of this is that they could be filled to an arbitrary pressure to achieve the desired "stiffness". However, the pressure would vary with temperature and leakage could be a problem, so it would be necessary to incorporate some sort of pump. This adds both complexity and weight to the design. There is also the risk of a "flat" from which there would be no recovery. This concept was hence discarded.

Springs within the Wheels

Springs within the wheels allowing deflection in all directions would greatly reduce the impact felt by the central body. In this case, significant displacement of the central body

relative to the wheels would need to be allowed for in all three axes. Concepts were generated to deal with this, but they would be time-consuming to develop in the detail design phase. To avoid undesired oscillations, the springs would need to be coupled with some sort of shock absorber, further complicating matters. For these reasons, this idea was also discarded.

Low-Deflection "Cushion"

This concept involves incorporating a "cushion" of flexible material (such as rubber) or elastic tubing between the inner cylinder and inner shell of the wheel. Because the cushion would be more rigid and shock absorbent than springs, this idea was selected to develop in more detail.

Many materials and geometries were considered, and it was finally conceived to create a cushion by filling the entire unoccupied wheel space with some type of foam. This way, the otherwise empty area of the sphere will be used completely for cushioning, and the load will be distributed more evenly. This concept is depicted in *Figure 11.* Because foams can be produced with an enormous range of mechanical properties, it is possible to find or custom-order the right foam for the application. The ideal foam would be lightweight, highly shock-absorbent, and resilient to multiple impacts.

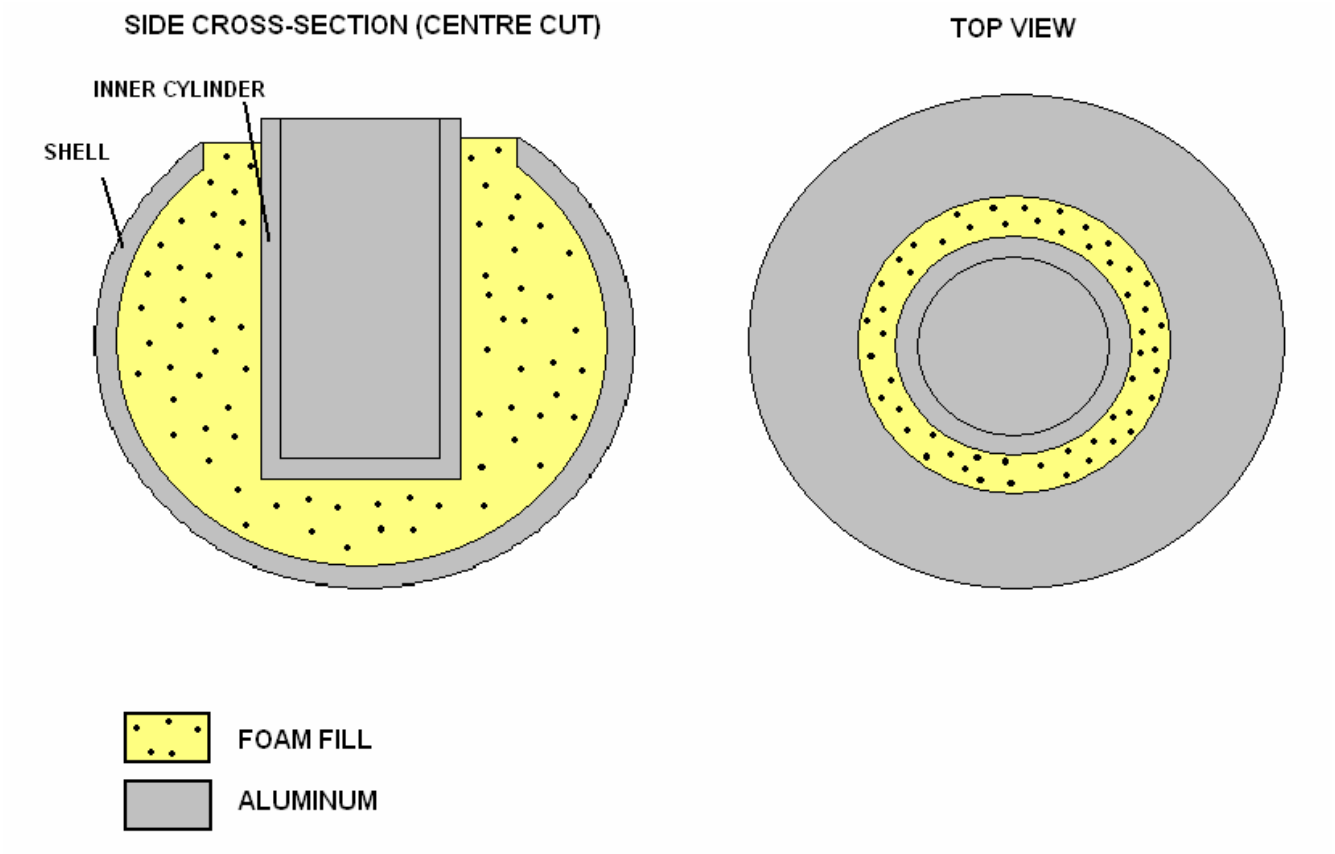

Figure 11: Foam fill concept

The same foam used to replace air in pneumatic tires to make them flatproof (lightweight polyurethane) was first considered for the cushion material because of its shock absorbing properties. After consultation with two experts on the subject at *Air Free Tires, Inc*. and *Arnco, Inc*, it was realized that a better foam for the application would be a cold curing urethane which would bond to the metal. Products from the company *Smooth-On Inc.,* were recommended, and the product *Foam-IT™ 8* was selected to design around, This foam is created by mixing two liquid compounds and allowing them to expand and cure. The density of the foam under consideration is ρ_{cush} = 120kg/m^3; other technical data is included in *Appendix II*.

To create the cushion, the inner cylinder would be fixed in place relative to the shell (which would already be coated with rubber). For these purposes, it may be beneficial to begin with a cylinder of extended length; the extended portion can be used for clamping during this process and machined off later. The liquid compound for the foam can then be poured in. This type of foam typically takes one to two days to cure, after which it will be bonded to the inner shell and cylinder. Note that the portion of the inner cylinder in contact with the foam would need to be completely sealed.

One potential problem with this configuration is that the shear stress may break the bond between the foam and the metal if too great a torque is applied. Some slip would consequently be possible between the foam and the metal as torque is applied to the cylinder. To prevent this, several small rods could be welded to both the inner wall of the shell and outer wall of the wheel cylinder, rounded at the tips to avoid tearing of the foam. These rods would prevent motion of the foam relative to the shell and cylinder.

Unexplored Potential

Late in the course of the design, an interesting suspension rubber suspension concept from *ROSTA Inc.* was discovered. The suspension rubber exhibits spring, damper *and* bearing properties. However, it was too late in the course of the design to thoroughly look into this concept. It is recommended that this idea is considered in more detail before the design is finalized. Details can be found at http://www.rostainc.com/PDFs/KAP01_EN.PDF .

3.2 – Wheel Coupling to Central Body

The end cylinder (fixed to the central body) must be able to rotate freely about the wheel inner cylinder (fixed to the wheel). Bearings are located near the flat face of the wheel to achieve this, depicted in *Figure 6*. The bearing selection process is discussed further on. Power will be transmitted from the motor and transmission to **Shaft A** of the wheels, providing some additional coupling support the nature of which is as of yet unknown.

3.3 – Central Body

The weight of the central body at standstill is kept as low as possible for stability. The core components and instrumentation will be almost entirely contained in the bottom half of the central body, leaving the top half for mission-specific equipment.

3.3.1 - Preliminary Dimensions

From the side view cross-section, the entire body must have a significantly smaller radius than that of the wheel, i.e. it must be contained within a circle of radius R_B (to be determined later on). A circular cross-section is not feasible if using rigid solar panels. However, the current flexible cells available provide much less power for a given area (Krauter, 2006). Thus, it was decided that the cross-section of the central body should have a regular polygon shape. All sides can be covered with solar panels.

The goal of the design was to maximize the body volume for storage capacity, and to maximize the surface area for solar energy absorption. For a given length, the greatest body volume is achieved by maximizing the cross-sectional area, and the greatest surface area is

achieved by maximizing the perimeter. Note that both the maximum cross-sectional area and maximum perimeter occur for a circular cross-section, i.e:

$$A_{X_{max}} = \pi \cdot R_B^2$$

$$A_{A_{max}} = 2 \cdot \pi \cdot R_B^2$$

Practically speaking, the polygon should have at least four sides, as shown by the square in the right of *Figure 12*. This is probably the simplest concept to develop, but a lot of potential body volume and surface area is given up. The effect of increasing the number of sides is made apparent in *Table 2*. Both the cross-sectional areas (directly proportional to volume) and surface areas (directly proportional to solar power) are calculated and shown as a percentage of the maximum values. A unit radius of 1 was used to generate the table, since the ratios of interest are independent of the radius.

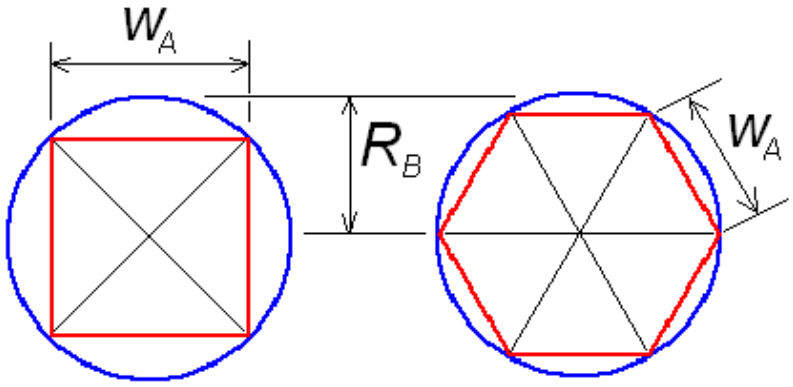

Figure 12: Regular polygons fit within circle of R_B

Num. Sides (N)	X-Section Area (A)	% Max. X-Section Area	Surface Area	% of Max. Surface Area
4	2.0000	63.66%	5.6569	90.03%
6	2.5981	82.70%	6.0000	95.49%
8	2.8284	90.03%	6.1229	97.45%
10	2.9389	93.55%	6.1803	98.36%
12	3.0000	95.49%	6.2117	98.86%
14	3.0372	96.68%	6.2306	99.16%
16	3.0615	97.45%	6.2429	99.36%
18	3.0782	97.98%	6.2513	99.49%
20	3.0902	98.36%	6.2574	99.59%

Table 2: Polygon area and solar panel area for different number of sides

It is clear that more sides results in a greater volume and greater panel area, which is desirable. However, fewer sides results in a simpler design, saving time and money, and likely leading to a more robust structure. The complexity of adding more sides is not really worth the small amount of volume and surface area gained. Additionally, the usable volume increase is in practice less than the actual volume increase, because fitting components in the angled sides is difficult.

For structural stability, it is desirable to have a central solar panel attached to the central body, and to have vertical symmetry about the centre of its length. It follows that there must be an odd number of polygon sides. The number of sides selected for the central body cross-section, i.e. the number of solar panels, is chosen to be $N_P = 9$, considered to provide a good compromise between complexity and space.

Based on the test environment, the vertical clearance between the ground and central body when ATOM is positioned on a flat surface was set at c_G = 55 mm. The maximum allowable radius for the central body is hence R_B = 107.4 mm. For successful deployment of the panels (for no chance of them scraping the ground), based on *Figure 15*, the clearance between the ground and the central body should be at least

which works out to be 44 mm. This is within the selected clearance of 55 mm.

We want the body to be as long as possible without scraping the ground during normal operation. Based on the test environment, a maximum incline angle of φ_{slope} = 20 degrees between the two wheels is assumed. From the geometry in *Figure 13*, the maximum length between wheel centres is calculated from:

$$L_{cc} := 2 \cdot \left(R_B \cdot \tan\left(\frac{\phi_{slope}}{2}\right) + \csc\left(\frac{\phi_{slope}}{2}\right) \cdot \left(R_W - \frac{R_B}{\cos\left(\frac{\phi_{slope}}{2}\right)} \right) \right)$$

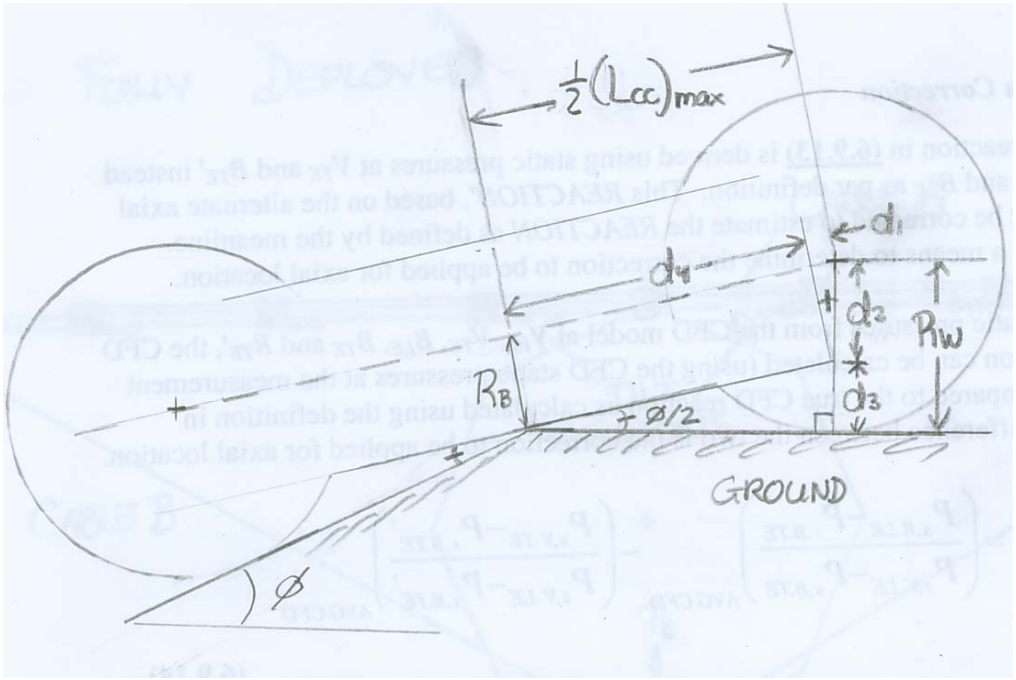

Figure 13: Maximum length between wheel centres

3.3.2 – Structure

The structure of the central body frame is shown in *Figure 9*. The walls can be made of bent sheet metal, with the shelf and shelf supports on the upper part welded in position. A wall thickness of 3 mm was selected.

The central body frame can be bolted to the end caps as shown in *Figure 14*. The end caps themselves are connected to the inner cylinder (this can be achieved through welding), which exhibits a rotary connection with the wheel.

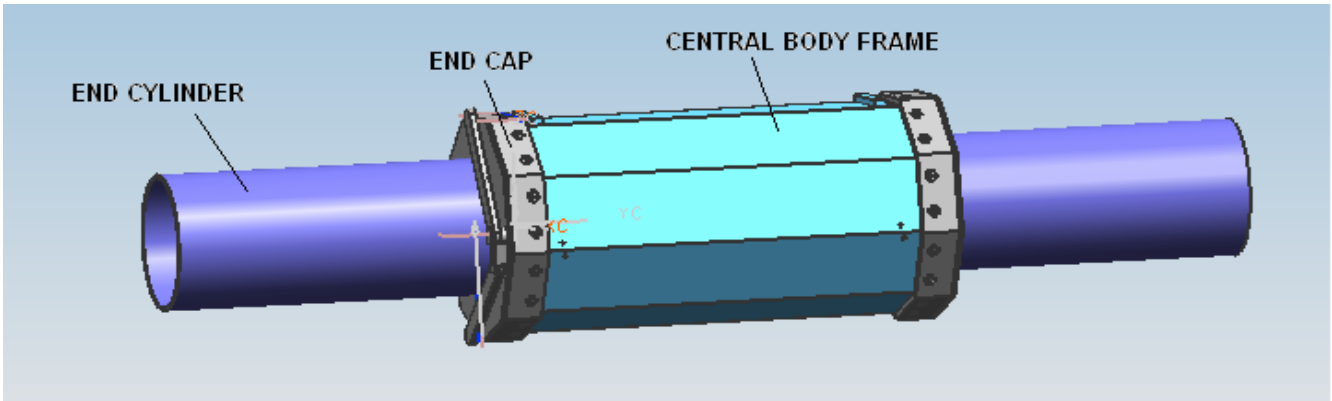

a) Assembled

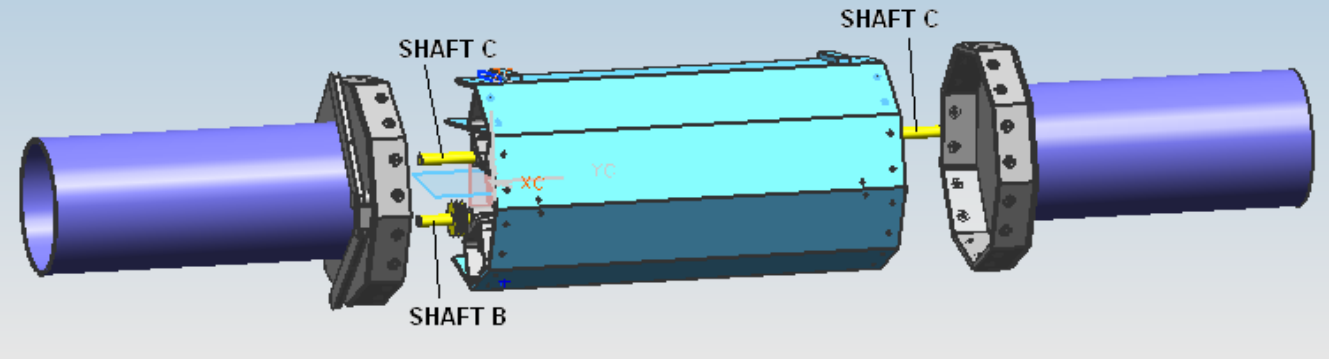

b) Exploded view

Figure 14: Central body assembly with wheels removed for visualization

Aluminum was the first choice for the end cap material because of its high strength to mass ratio. However, it was advised by a licensed welder that a more precise assembly would be possible if steel were used instead. This will also give greater strength to the part.

The end of the central body and the parallel inner face of the end cap were axially offset by 10 mm in the design to allow sufficient space for a weld between the end cap face and the end cap walls. In addition, a clearance of 1 mm was left between the outer wall of the central body and inner wall of the end cap on each side of the polygon for ease of assembly.

3.3.3 – Additional Major Dimensions

The thickness of the end cap wall dictates the clearance between the central body frame and the solar panels, which can be used for bolt heads (allowing components to be fixed to arbitrary locations in the central body), torsion hinges, and solar panel wiring. To provide sufficient space, the cap wall thickness was chosen to be 5 mm; with the clearance between the central body and end caps set at 1 mm. The result is a total gap of 6 mm between the panels and the central body.

The selected solar cells are only 140 μm thick, but the panels require a baseboard on which the connections between panels will be made, as well as a transparent pane on top to protect the cells from the elements (namely dust). It is assumed that this combination will be no greater than 10 mm thick. The prototype was therefore designed with a panel thickness of t_P = 10 mm. It is likely that the panels will not be quite so thick; the only effect this will have on the design is an increased clearance between the central body and ground, which is a positive result.

To allow greater room for the central body and to create an easy-to-work-with flat surface, the spherical wheels can be machined at one end to have a flat surface as shown in *Figure 15*, with the radius at the position of the cut as great as R_B. Based on the equation of a circle, the minimum horizontal distance between wheel centre and wheel cut is d_c = 121.8 mm.

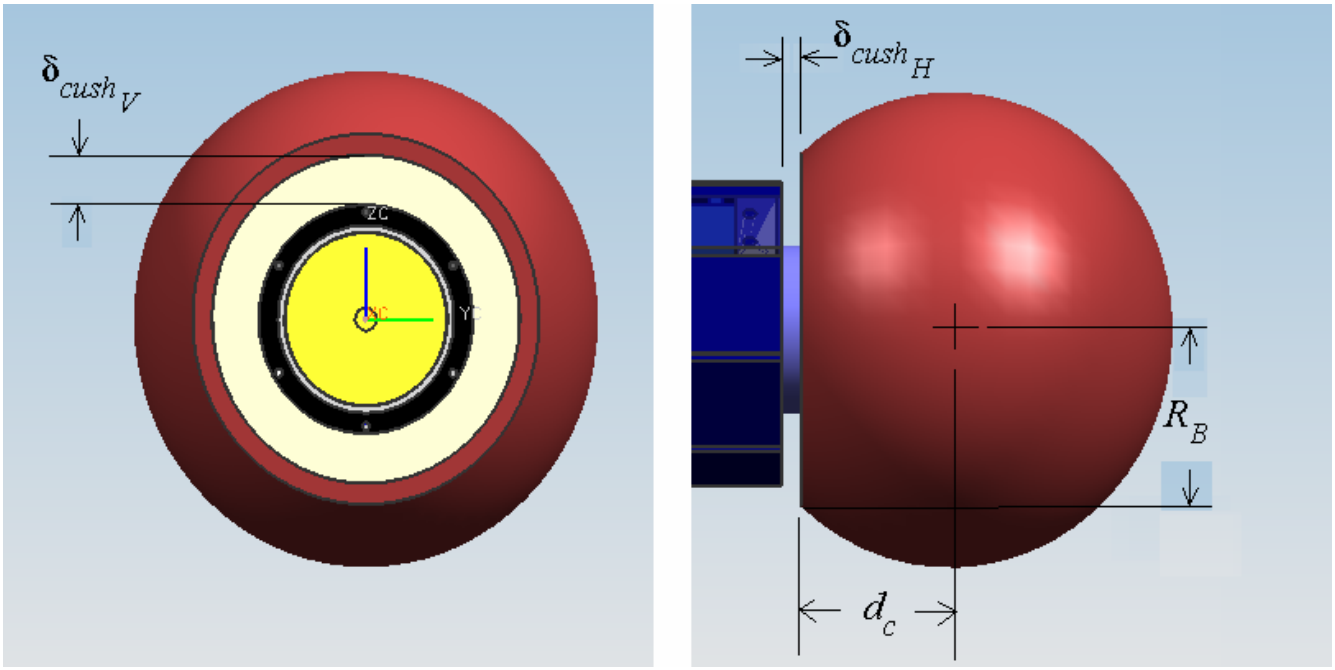

(a) Radial (b) Axial

Figure 15: Maximum desirable cushion deflections

The allowable radial deflection of the cushion before the inner cylinder contacts the shell, and the axial clearance between the inner wheel and the edge of the solar panels (see *Figure 15* for a schematic) were designed to be at least:

$$\delta_{cush_V} := 0.02$$

$$\delta_{cush_H} := 0.03$$

3.3.4 - Mass

The equation for a spherical cap of the geometry shown in Figure 16 is:

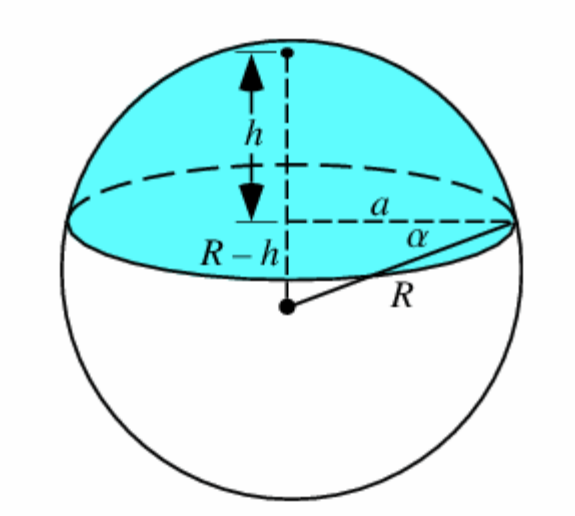

Figure 16: Spherical cap of height h

Image source: http://mathworld.wolfram.com

Based on this equation, the inner volume of the wheel (that contained by the shell), the volume of the shell itself, and the volume of the rubber layer were calculated and multiplied by their respective densities to obtain their masses.

The total volume of the cushion is the wheel volume enclosed by the shell minus the volume of the inner cylinder contained in the wheel. The mass and density were used to calculate the cushion mass, which is less than 2 kg. The total mass of the wheel (excluding the inner cylinder) includes the mass of the rubber, shell, and foam fill. We find that m_W = 7.25 kg.

Because a progressive approach is being used with regards to instrumentation and mission goals, a fair amount of space will be left in the ATOM prototype to add instrumentation/equipment. Thus, the potential mass is much greater than the design mass. To be conservative and design so ATOM is capable of being "packed to the maximum", the body was modeled as having a solid composition of aluminum. The resulting overall mass, referred to as "full-capacity mass", is approximated as m_{full} = 65 kg. This mass is the one used for impact analysis and drive power calculations.

The actual prototype will be significantly lighter because there will be a fair amount of unused space between components and equipment. In addition, most of the components will be of lower density than aluminum. By over-estimating the weight, a safety factor is inherently applied.

3.4 – Transmission

The transmission system is comprised of the electric motor and the interface between the motor and shafts **A**, **B**, and **C** (i.e. any mechanisms required to transmit power from the electric motor to the desired application, including any speed reducers). This system is yet to be designed; the space within the end cylinder (of approximate length 265 mm and radius 55 mm) has been allocated for a transmission system. The transmission could extend into the central body if more space is required. The transmission on ATOM's legside must be designed to achieve transition between the following modes.

3.4.1 - Drive Mode

In this mode, shown in *Figure 17,* the motor is engaged with **Shaft A**; shafts **B** and **C** are locked relative to the central body. When run, the motor will apply torque to **Shaft A** for the purposes of turning the wheel relative to the central body (driving) and causing the appropriate acceleration as dictated by the control system (balancing).

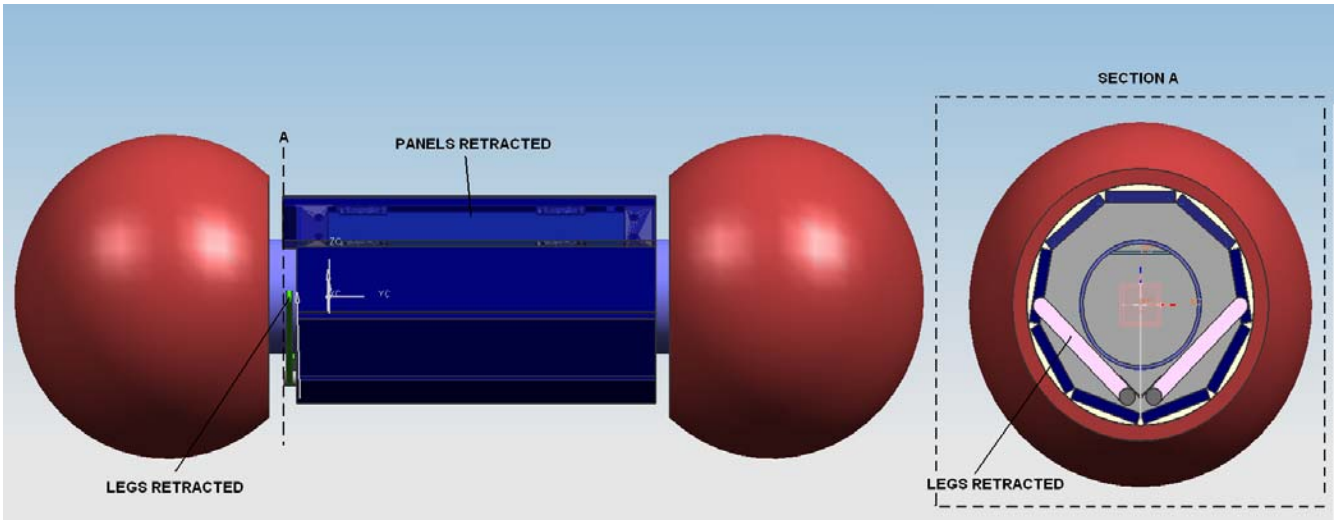

Figure 17: Drive Mode

3.4.2 - Charge Mode

To transition to this mode, seen in *Figure 10*, the motor must be disconnected from **Shaft A** and **Shaft A** locked relative to the central body. **Shaft B** must *first* be unlocked relative to the central body, followed by **Shaft C**, leaving them free to rotate about the central body. The tension in the **B** and **C** cables is relaxed at the unlocking of these shafts. As a result, the strong torsion springs at the leg hinges will cause the legs to spring out and hold the central body in a fixed position with respect to the ground (*Figure 10*). The torsion springs at the solar panel hinges will cause the solar panels to raise to their charge position (*Figure 10*). Note that the motor is not engaged with any shaft in this mode.

3.4.3 – Panel Retraction

The transition to this mode involves engaging the motor with **Shaft B** such that running the motor will cause a clockwise rotation of the shaft with respect to *Figure 11*. At this rotation, the **B Cables** will be held in tension and wrapped around **Winch B**, causing the panels to wrap back around the central body.

One method to determine when to transition to the next mode involves measuring the total rotation of **Winch B** relative to the central body from the charge mode position. Once the disk has rotated enough to bring the panels back to the drive mode (this will be a fixed amount), an immediate transition to the leg retraction mode can take place. There are many other possibilities for achieving this.

3.4.4 – Leg Retraction

To transition to this mode, **Shaft B** must *first* be locked in place relative to the central body, *and then* the motor must be disconnected from **Shaft B** and engaged with **Shaft C**. The function of this mode is similar to that of the leg retraction mode, with all references to **B** replaced by **C**, except the result is the retraction of the stabilizing legs instead of the solar panels. The transition from the leg retraction mode back to the drive mode can be facilitated in the same way as that from the panel retraction mode to the leg retraction mode.

3.4.5 – Transition from Mode 4 to Mode 1

This transition requires *first* locking **Shaft C** in place relative to the central body, *then* disconnecting the motor from **Shaft C** and engaging it with **Shaft A**.

3.4.6 – Transmission Requirement Summary

A process map of the required transmission cycle is seen in *Figure 18*, with the modes seen in the rectangular boxes and the transmission functions (transitions between modes) in the trapezoids. Note that the motor is fixed relative to the central body at all times.

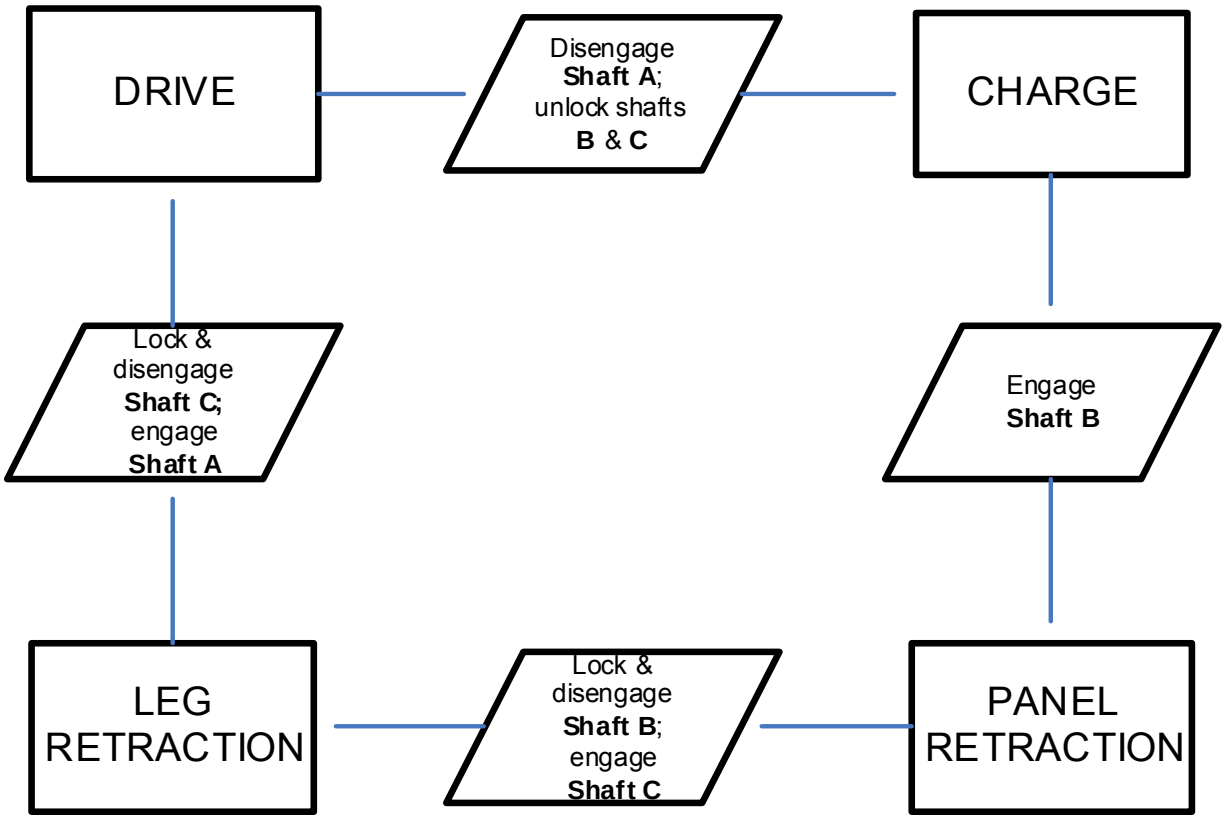

Figure 18: Transmission process map

The transmission should be lightweight with low power and space requirements. It may turn out to be more practical to include additional motors to run shafts **B** and **C**, if this will involve less weight, or if a transmission system would be too complex or bulky. Another

option would to be to split the tasks between both motors (i.e. use one to run **Shaft B** and the other for **Shaft C**). Concept generation has taken place regarding the transmission system; however it is not sufficiently developed to be presentable in this report.

The transmission on the other side of ATOM (non-legside) would need only to transmit power between the motor and **Shaft A**.

3.5 - Instrumentation

ATOM's instrumentation is divided into two categories: core instrumentation, which is permanent instrumentation necessary for basic operation (contained in the lower half of the central body), and mission-specific instrumentation, which for the Strawman task will be surveying equipment (contained in the upper half of the central body).

3.5.1 - Core Instrumentation

Danielle Nasrallah's model of ATOM requires that the exact orientation of the central body be known, possible in theory through the use of accelerometers.

It is best to use as many types of instrumentation as possible, and determine the error in each from their feedback. A consultation was held with a graduate student, Phillipe Cardou, who has done Ph. D work on such instrumentation. His suggestion was to use a progressive approach, i.e. begin with minimal instrumentation and add more if prototype tests show inaccurate results. The following types of sensors were considered.

Encoders

Encoders could be used to measure the rotation of the wheels with respect to the central body. These are often used in vehicular applications to determine the kinematic properties of the system.

Unfortunately, even if the instruments are working perfectly, inaccuracies arise in this procedure due to wheel slippage. The inaccuracies will be even greater in ATOM, because the spherical wheel shape implies that the contact point with the ground is not necessarily at the wheel centre. The distance between the axis of rotation and the contact point varies over time, thus the radius of curvature is unknown and the encoder information is not extremely useful on its own.

Accelerometers

Accelerometers, which measure tilt angles with respect to gravity, give very accurate measurements but have a rather low response time. Another problem is that they are unable to differentiate between the acceleration of gravity and the horizontal acceleration of the body, and so are inaccurate during system acceleration.

Gyroscopes

Gyroscopes measure the tilt around a certain axis, and typically have high accuracy and excellent response time, but tend to drift over time.

Selected Instrumentation

The best method is to use a combination of accelerometers and gyroscopes, and use an algorithm providing feedback based on the output from both. There are a number of

commercially available units that incorporate both. Because it is important to know the exact pose and heading of ATOM, tri-axial versions of these devices were considered. The system selected to design around was the *3DM-GX1® Gyro Enhanced Orientation Sensor* from *MicroStrain Inc.* This device combines three accelerometers, three gyroscopes, and three magnetometers, and comes with software determining the inertial properties at any given time based on all nine feedbacks. Temperature correction factors are also accounted for.

The entire unit is quite small, measuring 64 x 90 x 25 mm. The technical data sheets are included in *Appendix II*.

3.5.2 - Mission-Specific Instrumentation

In addition to the core ATOM components, this mission requires equipment to perform topographical surveying. For the prototype, a GPS unit will probably be incorporated for these purposes. Accuracies in the range of centimeters can be achieved if communication is possible between the GPS unit and a fixed local station of known location. In addition to being used for surveying, the GPS equipment could also contribute greatly to the feedback indicating ATOM's pose, heading, speed, and acceleration. However, although work is being done to set up a satellite system on Mars for GPS positioning, this is currently not feasible on Mars.

3.6 – Power

ATOM must be capable of operating for long periods without human intervention, so a self-rechargeable power system had to be incorporated in the design. Solar power was selected as the energy source because the equipment is commercially available with known characteristics. In addition, the rovers currently on Mars (*Spirit* and *Opportunity)*, have demonstrated the feasibility of solar-powered missions. They have in fact spectacularly exceeded their expected mission life of 90 days, having been in operation for well over a year and are still running (Ratnakumar, 2006). The major issue with the use of solar energy for ATOM is that the nature of the design gives a low surface-area to volume ratio.

Because ATOM's shape does not expose a large amount of the surface area to the sun, the solar panels are designed to deploy into a single plane, as shown in *Figure 14(b)*. This is the charge mode of ATOM, when the rover is not in motion. It is also desirable that the deployed surface be capable of tilting to better face the sun. If additional power turned out to be required, another retractable layer of solar cells could be included.

3.6.1 – Power Requirements

ATOM requires power to operate the following components:

- The drive/transmission system
- The on-board computer
- The communication system
- Mission-specific equipment
- The sensors

The total power requirements as well as the power load distribution will depend on the mission and on the mass of the robot.

Nominal Drive Power

To estimate the torque required to turn the wheels, torque fluctuations due to balancing are ignored, and the wheels are assumed to be conventionally driven. A design speed of about 0.5 m/s is used, and at this speed the dynamic effects (e.g. inertia, air resistance) can be neglected (Iagnemma, 2004).

The model to follow assumes that the wheels are rigid relative to the terrain, which is valid considering the high compressive modulus of the rubber layer. *Figure 19* defines the geometry and stress locations.

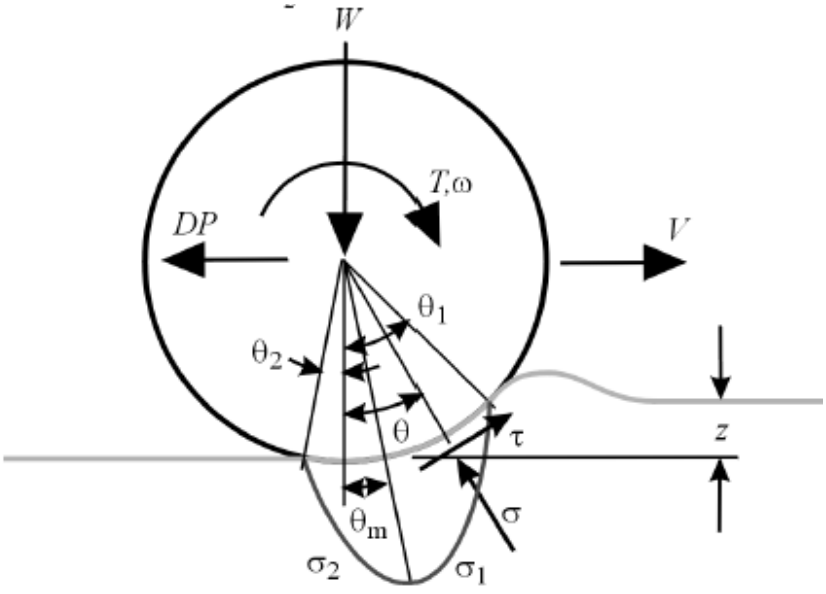

Figure 19: Wheel drive power model

Based on the Martian terrain data presented previously, the pressure sinkage moduli and shear deformation modulus are, respectively, k_c = 1000 kPa/m^{n-1}, k_φ = 1520 kPa/m^n, and k = 0.025 m. The cohesion is given as *coh* = 1600 Pa, the cohesion angle as φ_c = 20 degrees, and the sinkage exponent as n = 1.1. The maximum sinkage (at θ_1) is given by:

$$z_0 := \left(\frac{3 \cdot \frac{m_{full}}{2} \cdot g}{b \cdot (3 - n) \cdot \left(\frac{k_c}{b} + k_\Phi \right) \cdot sqrt(2 \cdot R_W)} \right)^{\left(\frac{2}{2 \cdot n + 1} \right)}$$

From geometry, it can readily be shown that:

$$\theta_1 := arccos\left(1 - \frac{z_0}{R_W}\right)$$

For the analysis, θ_2 is assumed to be zero, as this angle is usually quite small in practice. For many soil types at moderate slip ratios, it can also be assumed that the angle at the location of maximum stress is (Kang 2003):

$$\theta_m := \frac{\theta_1 + \theta_2}{2}$$

From the geometry in *Figure 19*, the sinkage at the point of maximum stress (θ_m) is:

$$z := R_W \cdot (cos(\theta_m) - cos(\theta_1))$$

The maximum stress is given by:

$$\sigma_m := \left(\frac{k_c}{b} + k_\phi \right) \cdot z^n$$

Although ATOM is intended for no slip, in practice this is not realistic. The slip, defined by:

$$i = 1 - \frac{V}{R_{B\omega}}$$

is unknown. A conservative slip of i = 0.2 was selected for the model.

The maximum shear stress is given by:

$$\tau_m := \left((coh + \sigma_m \cdot tan(\phi_c)) \cdot \left(1 - exp\left(\left(-\frac{R_W}{k_s} \cdot (\theta_1 - \theta_m - (1-i) \cdot (sin(\theta_1) - sin(\theta_m))) \right) \right) \right) \right)$$

The following gives the required wheel torque in compliance with *Figure 19*:

$$T_{wheel} := evalf\left(\frac{R_W^{\,2} \cdot b}{2} \cdot (\tau_m \cdot \theta_1 - coh \cdot \theta_m) \right)$$

where b is the wheel width for conventional wheels. Since ATOM's wheel is spherical, this width is assumed to be the width of wheel in contact with the ground, approximated as the wheel radius.

The power required from each motor is calculated from:

$$P_{motor} := T_{wheel} \cdot \omega_{wheel}$$

and the total drive power required will be double this amount. Based on the preceding model equations, using the gravitational acceleration on Earth (where the prototype will actually be driven), it is found that the total drive power, torque, and angular speed under these conditions are P_{drive} = 35 W, T_{wheel} = 4.5 Nm, and ω_{wheel} = 3.85 rad/s.

In reality there will be some losses through power transmission.

Hill Climbing Drive Power

The maximum design incline of φ_{climb} = 45 degrees is used to determine the maximum required hill-climbing power, calculated from:.

$$P_{climb1} := m_{full} \cdot g \cdot \sin(\phi_{climb}) \cdot V_{climb};$$

ATOM will be designed to climb at a rate of V_{climb} = 0.1 m/s under these conditions. The above is the power required to lift the vehicle ONLY, and does not consider the wheel-terrain interaction. Thus, to estimate the total power required for climbing the hill, the ordinary drive power required at this speed must be added. Reevaluating the drive power, changing the speed from 0.5 to 0.1 m/s and assuming a higher slip of i = 0.4 for hill climbing, the total climb power is P_{climb} = 70 W. It is found that the angular wheel speed is ω_{wheel} = 1 rad/s, and the required wheel torque is T_{wheel} = 6.7 Nm. Again, in reality there will be some losses through power transmission.

Non-Drive Power

The power of the remaining electronics (sensors, CPU, transmission) is estimated as 50 W, based on similar robots and the power breakdown for the current Mars rovers, *Spirit* and *Opportunity*. The total nominal operating power will driving is hence 85 W.

3.6.2 – Energy Source

ATOM must be capable of operating for long periods without human intervention, so a self-rechargeable power system had to be incorporated in the design. Solar power was selected as the energy source because the equipment is commercially available with known characteristics. In addition, the rovers currently on Mars (*Spirit* and *Opportunity)*, have demonstrated the feasibility of solar-powered missions. They have in fact spectacularly exceeded their expected mission life of 90 days, having been in operation for well over a year

and still running (Ratnakumar, 2006). The major issue with the use of solar energy for ATOM is that the nature of the design implies a low surface-area to volume ratio.

Because ATOM's shape does not expose a large amount of the surface area to the sun, the solar panels are designed to deploy into a single plane, as shown in *Figure 10(b)*. This is the charge mode of ATOM, when the rover is not in motion. It is also desirable that the deployed surface be capable of tilting to better face the sun. If additional power turned out to be required, another retractable layer of solar cells could be included.

Typically, 36 cells are connected to form a solar array; this is possible if each of ATOM's nine solar panels is comprised of four solar cells.

Daily Energy Captured

The solar energy available on Mars is calculated based on the irradiation and daylight plots shown in figures 4 and 5, respectively. Since ATOM is designed for Spring/Summer missions, we consider this part of the curve, noting the average irradiation per day is about 3500 W-hr/m^2.

ATOM is assumed to be in charge mode for the 6 peak hours of the day. Note that ATOM is also charging when its arrays are not deployed, only with less surface area. Based on *Figure 5*, it is thus assumed that ATOM's deployed panels will be exposed to 75% of the average daily irradiation, which works out to be is 9.45 MJ/m^2. The total panel area when deployed is approximately 0.2 m^2. However, the area may not be completely covered in solar cells, thus this area was reduced by 10% to calculate the total daily irradiation energy experienced by the panels as E_{irr} = 2 MJ.

It is noted that the efficiency of photovoltaic cells increases with decreasing

temperatures, and typically exhibits a peak efficiency between 150 and 200 K (Krauter, 2006). The temperatures on Mars near the equator, where the mission is assumed to take place, are in the range of 200 - 250 K, close to the peak efficiency temperature.

The Mars rovers *Spirit* and *Opportunity* were powered with Ultra Triple Junction (UTJ) solar cells from *Spectrolab, Inc.*, and had a 27.5% beginning-of-life efficiency. UTJ solar cells from the same company have been considered for ATOM, which have a quoted efficiency of 28.3%. The solar cells used for future missions should thus be at least as efficient as those from previous ones. To be conservative, considering dust accumulation that may reduce the solar cell efficiency, the efficiency of the solar panels is taken as η_P = 20 %.

At this efficiency, the energy during charge is 0.4 MJ. Note that the battery characteristics may not allow 100% charging capabilities at all times, so some of the energy may be wasted. Note also that during the winter seasons ATOM would still be functional, but charging time required would be longer for a given operating time.

3.6.3 – Deployment/Retraction Mechanism

Three main methods were considered to deploy the solar arrays, as described below. Note that the original concept involved panel symmetry about the vertical, as shown in *Figure 20*. When fully deployed, the flat solar array would be able to pivot about the highest point, so that the panels could face the sun as directly as possible. If an octagonal geometry were used, a maximum tilt angle of 22.5 degrees would be achievable. For greater tilt angles, the central body itself would need to be tilted. Development of the tilting mechanism turned out to be beyond the scope of the current work.

Cable-Pulley Link Alignment System

The concept is illustrated in *Figure 20(a*). In this design, **Cable A** would be pulled in the direction of V_c by a tension provided by an internal motor. The "link aligners" would be pulled over the joints, causing them to "straighten out" into the position shown in *Figure 20(b)*. Although the sketch implies each link aligner would pass over its joint at the same time, the current concept is to have **Joint 3** first covered by a link aligner, then **Joint 2**, then **Joint 1**. This results in a more predictable motion, and is achievable through different geometries and positions on **Cable A** for the link aligners. Note that **Cable A** actually represents four cables, one on either side of the cross-section shown, on either side of the central axis.

Actuated Joints

In this design, the joints will be actuated, and under-actuation would be exploited during retraction so the links would "grip" the body. The gripping would be accomplished using a similar concept as used for the fingers of compliant-mechanism robotic grippers (Gosselin, 2006).

This concept was more complex than the link-alignment system from a power/electrical point of view, but most likely simpler from a mechanical viewpoint.

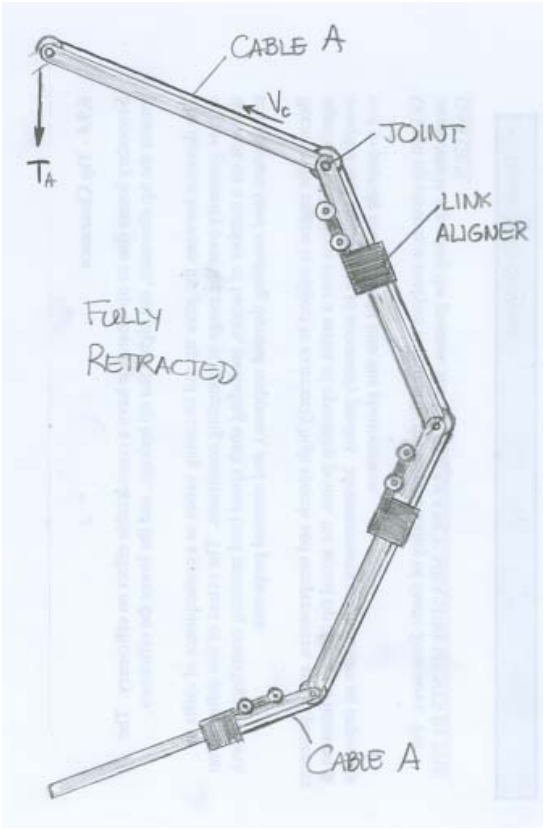

(a)

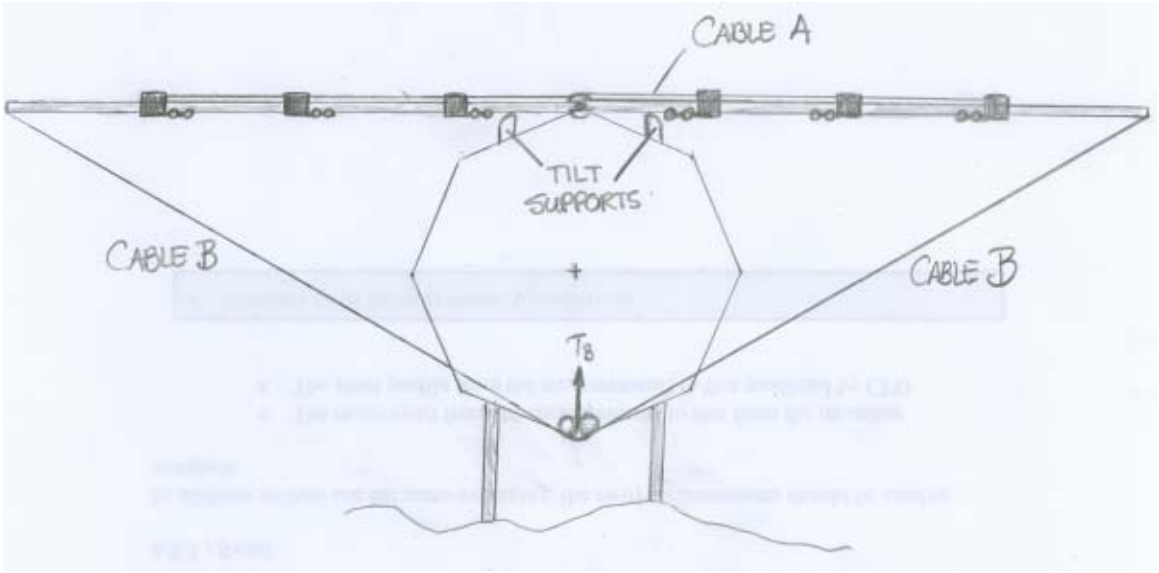

(b)

Figure 20: Link-Alignment concept (a) Deployment mechanism (b) Fully deployed position

Torsional Spring System

The final concept selected for the deployment mechanism was a spring-loaded hinge connection between the panels, as described in *Section 2.2* and depicted again in *Figure 21.* The advantage of this concept is that minimal power would be required to deploy the panels; the only power needed would be that used by the transmission system to unlock shafts **B** and **C** relative to the central body.

Thin but sturdy cables were desired to pull the solar panels and legs to the drive position (panels retracted). Both the **B** and **C** cables were selected as Part No. 2037SN from *Sava Industries Inc.*, and each cable is capable of withstanding 72.6 kg-force with no danger of breaking. This is well above the loads to be experienced by ATOM's cables. To ensure that the winches will always be rotated a certain amount to bring ATOM to its drive position. it is important that the axial distance between the winch disks is very close to the cable diameter. This ensures that the cable will always wrap around the same radial location. The selected cables are 1.17 mm in diameter, which was rounded up to 1.5 mm to allow some tolerance, reducing friction.

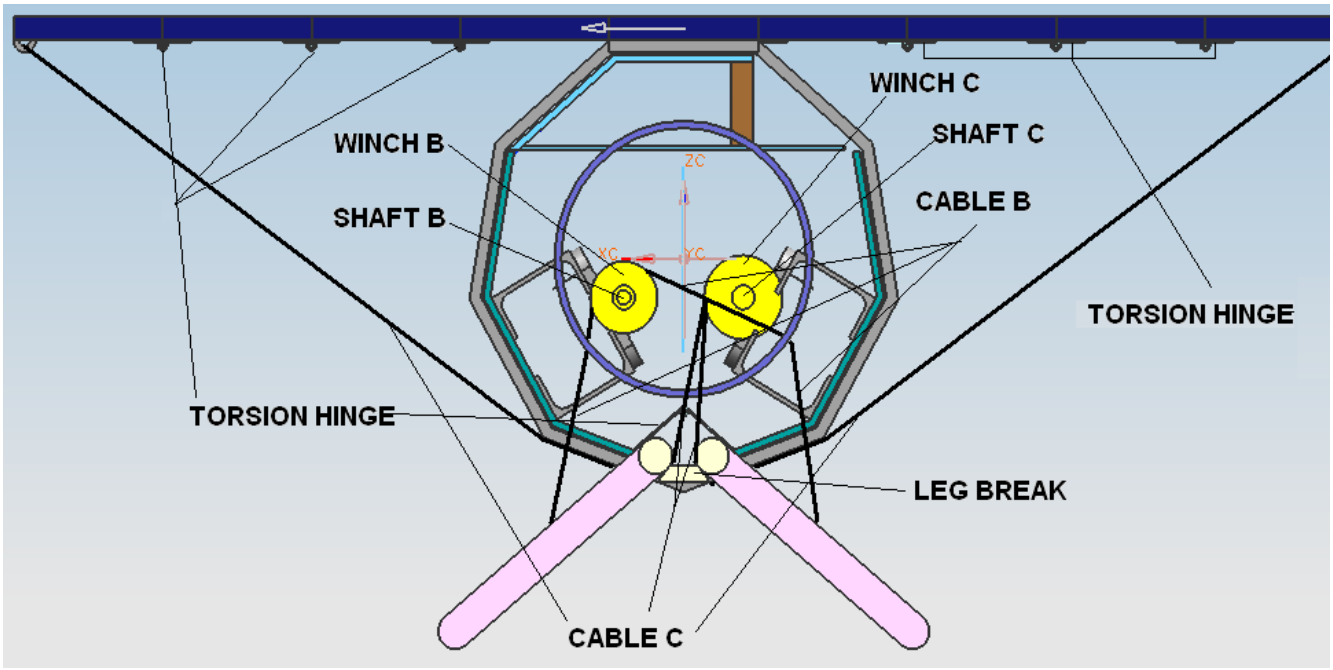

Figure 21: Array deployment/retraction mechanism

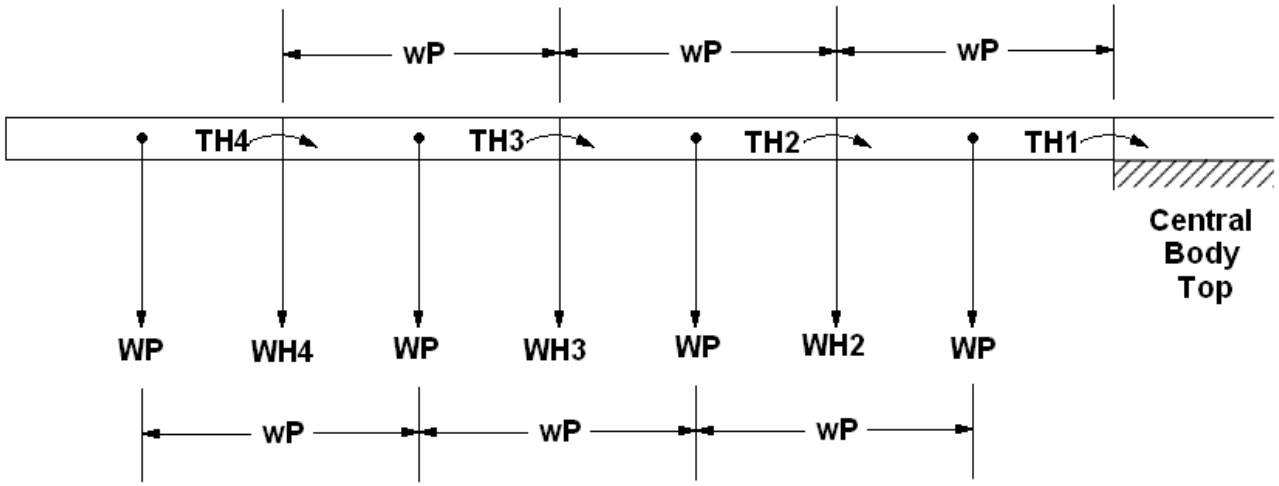

Figure 22: Free body diagram of panel hinge forces, left side

Based on the free body diagram in *Figure 22*, if two torsion hinges are used for each panel connection, for equilibrium conditions, it is required that:

$$T_{H_2} := \frac{1}{2} w_A \left(\frac{9}{2} W_P + 2 W_{H_3} + 4 W_{H_4} \right)$$

$$T_{H_3} := \frac{1}{2} w_A \left(2 W_P + 2 W_{H_4} \right)$$

$$T_{H_4} := \frac{1}{4} w_A W$$

However, during the solar panel deployment, the torque in the springs must also overcome:

- The inertia of **Winch C** and **Shaft C**
- Friction opposing the deployment motion (from drag on the body frame and **Winch C**)
- Possible drag induced by wind

Although these effects are difficult to analyze precisely, they will be small. It is important that the torsion spring constant in the hinges be higher than that necessary to accomplish the task of deployment, but it should not be arbitrarily large because a higher torque implies higher acceleration; the panels will reach the deployed position at a higher speed, upon which they must suddenly be brought to rest by the angular constraints of the hinges (they cannot pivot beyond the horizontal position). Higher impact-type stresses will thus be experienced Higher tension in the **C Cables** during panel retraction also implies greater power during the procedure.

Note that the torsion springs to be implemented must be restricted from pivoting beyond the deployed (horizontal) position.

From *Figure 22*, the base of the solar panels would need to be able to withstand a bending moment equivalent to $T_{H.}$

3.6.4 – Energy Storage

Because solar energy is not constant or reliable, it is essential to have a good battery system to store energy and provide power when little or no irradiation is present. The ideal battery would be lightweight, fairly insensitive to charging cycles, and capable of operating at low temperatures. Lithium-ion and lithium thionyl-chloride batteries are under consideration for ATOM, as they exhibit these characteristics. The battery capacity and design will depend on the electrical load details which are yet to be determined. For the prototype design, the battery was modeled as the NCP551 battery from *Lithion Inc.*, the same company provided similar batteries for Mars rover missions.

Note that this battery is very expensive (approximately $4000), so it is recommended to use a battery of less capacity for the prototype. *Saft America, Inc.*, has been contacted regarding the use of its batteries; the representative believes that the company is well-suited to take part in the project, and is willing to determine battery specifications when further details are provided.

3.7 – Impact Analysis

Because ATOM is meant to be a robust robot capable of falling and flipping without damage, it is important to estimate the forces experienced during an impact in order to ensure that the stresses experienced by each component are well below the material yield limit.

Unfortunately, rubber is typically to stiff to significantly reduce impact. However, it will have the effect of distributing the force more evenly about the shell, resulting in a less concentrated load and, consequently, less stress in the shell than would be present without the rubber layer.

3.7.1 - Impact Model

For the impact model, we consider ATOM dropping from a height equal to the distance between wheel centers, i.e. L_{CC}, onto a rigid surface. Neglecting air resistance, it can readily be shown from basic kinematic equations that the speed of ATOM upon impact is:

$$V_{impact} := \sqrt{2}\,\sqrt{g\,L_{cc}}$$

Two orientations were considered for the analysis, both assuming symmetry about the vertical.

ATOM is upright when contacting the ground

This situation is depicted in *Figure 23(a).* Due to symmetry, the model can be reduced to *Figure 23(d).* Note that $k_{cush_V} = k_{cush}' = k_{cush}''$.

ATOM is rotated 90 degrees about the vertical when contacting the ground

This situation is depicted in *Figure 24(a).* Due to symmetry, the model can be reduced to *Figure 24(b).*

Figure 23: Upright drop

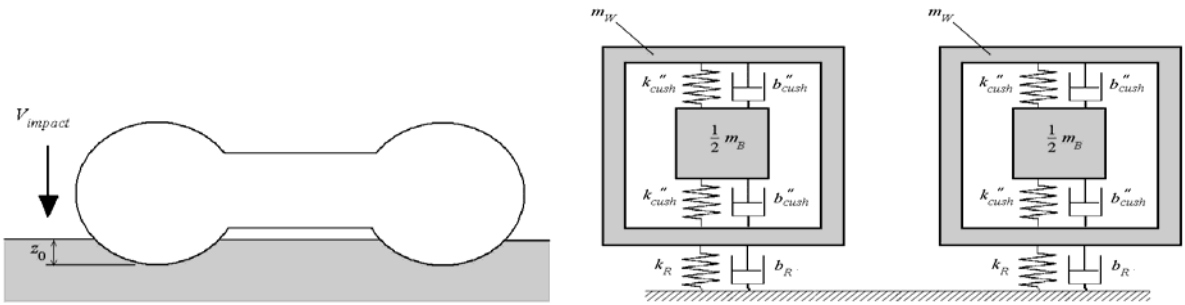

(a) Upright drop schematic *(b) Upright drop model 1*

(c) Upright drop model 2 *(d) Upright drop model 3*

Figure 24: Rotated drop

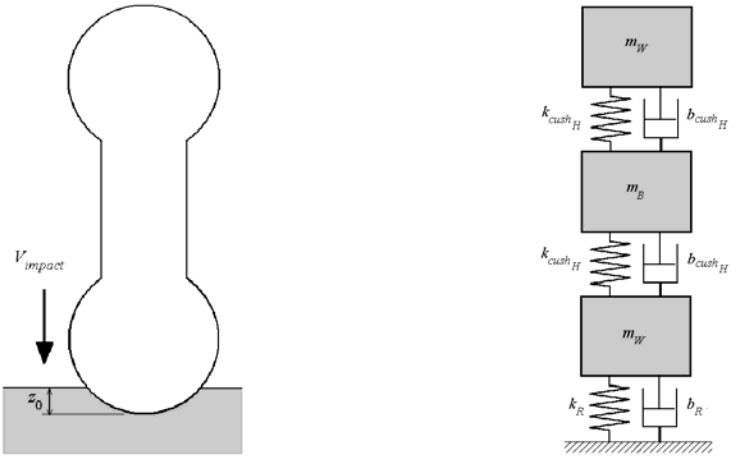

(a) Rotated drop schematic *(b) Rotated drop model*

For the impact analysis, *MATLAB* was deemed preferable to *Maple* for due to its system analysis capabilities. This setup allows two types of design approaches:

2) For a given set of material properties (coefficient of restitution, stiffness, and damping), the maximum forces experienced by the rigid bodies can be estimated
3) For a given maximum permissible impact, the required material properties can be determined, and from here appropriate materials and dimensions can be selected.

Spring & Damping Constants

The spring and damping constants depend on the geometry, material, and stress condition. Although the stress-strain characteristic of rubber is highly non-linear in tension, a linear approximation is reasonable in compression; *Figure 25* shows the compressive stress-strain behaviour of rubbers of varying hardness in compression. Based on this, it is reasonable to assume a constant stiffness for the rubber layer. The same assumption is applied to the foam cushion.

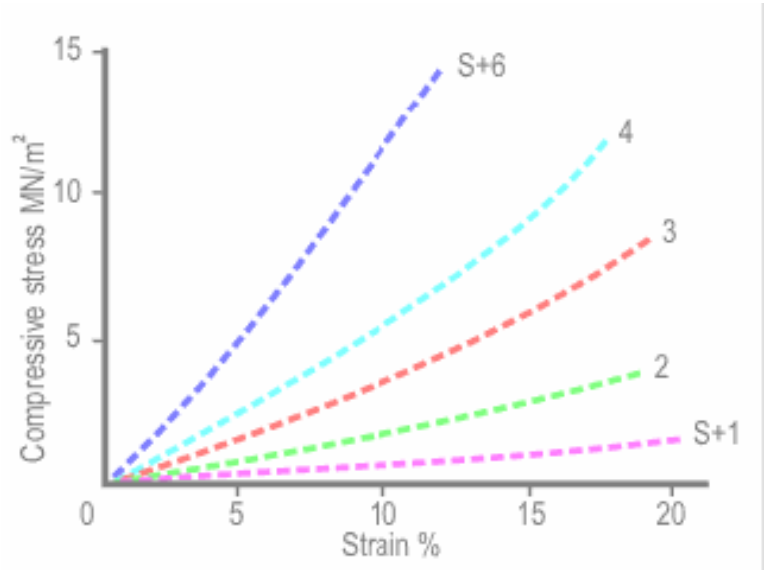

Figure 25: *Rubber stress-strain diagram in compression*

The spring constants of the rubber and cushion can therefore be determined based on the following equation:

$$k = \frac{EA}{t}$$

where *E* is the compressive modulus of the material, *A* is the effective area of compression, and *t* is the effective thickness of the compressed material.

Because of the complex geometry, several simplifying assumptions had to be made when determining the thickness. The complicated geometry of the foam cushion is dealt with by considering a pad of equivalent volume having uniform thickness. Although the upper portion of the cushion will be in tension and the lower in compression, considering just one pad in tension or compression is equivalent to considering two equal pads of half the volume. This is analagous to equating *Figure 23(a)* with *Figure 23(b)*. Note that a factor of 2 was introduced in the wheel spring constant in *Figure 23(b)* to account for the cushions in both wheels, which act as two equal springs in parallel (See *Figure 23*).

The maximum horizontal area within the wheel is taken because the equivalent stiffness is proportional to the area, and the maximum force experienced by the system masses increases with increased spring stiffness. Hence, this is a conservative estimate. In the case of the rotated drop, the maximum horizontal area is that of a circle of a radius equal to the inner radius of the shell. In the case of the upright drop, the maximum horizontal area equal to that considered for the vertical drop, minus the segment cut off at the end. This is calculated using the equation of the area of a circular segment, given in *Figure 26.*

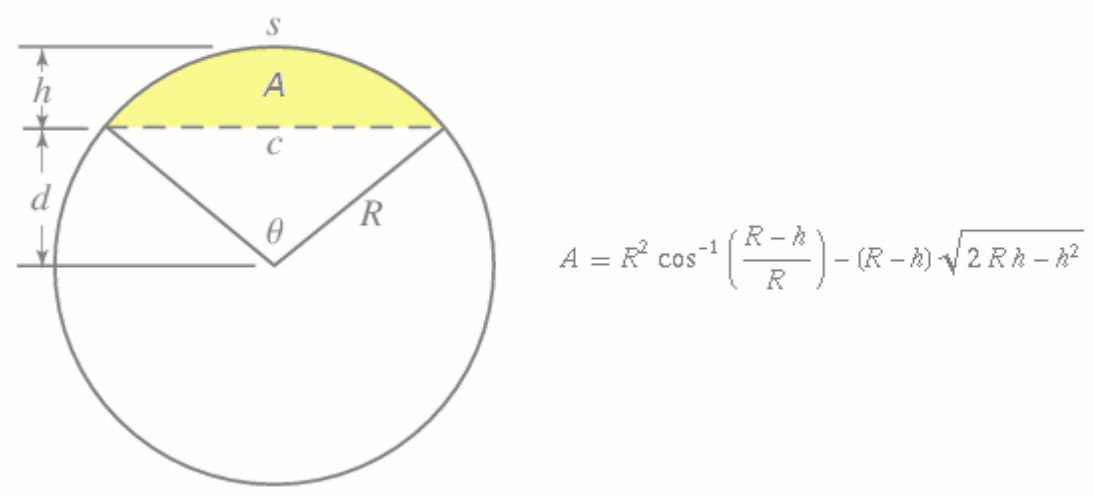

Figure 26: Circular segment area

To determine the thickness of the pads, the total volume of the spring is divided by the equivalent area. The equivalent spring constants turn out to be k_{cushH} = 4.3 x 10^6 and k_{cushV} = 4.1x 10^6.

For the rubber, the area is taken as the contact area of the wheel, i.e. surface area of a spherical cap of height equal to the depth of sinkage in the soil, z_0, (see figures 24) and radius equal to the wheel radius, R_B. To estimate z_0, the sinkage determined in the drive analysis is used. Because the sinkage will be even greater after a fall, this should be a conservative assumption.

The thickness was taken as the thickness of the rubber layer, i.e. 10 mm.

As the damping coefficients proved to be much more difficult to estimate, iterations of the code were performed over a range from 0 to 4000 Ns/m. The maximum resulting impact forces were taken as a conservative estimate.

For the upright drop, the equations of motion are:

$$2 \cdot m_W \ddot{z}_1 + (b_R + b_{cush_V})\dot{z}_1 + (k_R + k_{cush_V})z_1 = b_{cush_V}\dot{z}_2 + k_{cush_V} z_2 + 2 \cdot m_W g$$

$$m_B \ddot{z}_2 + 2b_{cush_V}\dot{z}_2 + 2k_{cush_V} z_2 = b_{cush_V}\dot{z}_1 + k_{cush_V} z_1 + m_B g$$

and for the rotated drop:

$$m_W \ddot{y}_1 + (b_R + b_{cush_H})\dot{y}_1 + (k_R + k_{cush_H})y_1 = b_{cush_H}\dot{y}_2 + k_{cush_H} y_2 + m_W g$$

$$m_B \ddot{y}_2 + 2b_{cush_H}\dot{y}_2 + 2k_{cush_H} y_2 = b_{cush_H}\dot{y}_1 + k_{cush_H} y_1 + b_{cush_H}\dot{y}_3 + k_{cush_H} y_3 + m_B g$$

$$m_W \ddot{y}_3 + b_{cush_H}\dot{y}_3 + k_{cush_H} y_3 = b_{cush_H}\dot{y}_2 + k_{cush_H} y_2 + m_W g$$

Until contact with the ground, all masses accelerate together, hitting the surface at V_{impact}. The following initial conditions are thus defined:

$$\begin{aligned} y_1 &= 0 \\ \dot{y}_1 &= V_{impact} \\ y_2 &= 0 \qquad & z_1 &= 0 \\ \dot{y}_2 &= V_{impact} \qquad & \dot{z}_1 &= V_{impact} \\ y_3 &= 0 \qquad & z_2 &= 0 \\ \dot{y}_3 &= V_{impact} \qquad & \dot{z}_2 &= V_{impact} \end{aligned}$$

Letting

$$\begin{aligned} x_1 &= z_1 \\ x_2 &= \dot{z}_1 \\ x_3 &= z_2 \\ x_4 &= \dot{z}_2 \end{aligned}$$

for the upright drop, and

$$\begin{aligned} x_1 &= y_1 \\ x_2 &= \dot{y}_1 \\ x_3 &= y_2 \\ x_4 &= \dot{y}_2 \\ x_5 &= y_3 \\ x_6 &= \dot{y}_3 \end{aligned}$$

for the rotated drop, each system can be defined by a state-space representation of the form:

$$\dot{\underline{x}} = \underline{A}\underline{x} + \underline{B}\underline{u}$$
$$\underline{w} = \underline{C}\underline{x} + \underline{D}\underline{u}$$

where, for the upright drop:

$$\underline{x} = \begin{bmatrix} x_1 \\ x_2 \\ x_3 \\ x_4 \end{bmatrix},$$

$$\underline{u} = [g]$$

$$\underline{A} = \begin{bmatrix} 0 & 1 & 0 & 0 \\ -\frac{k_R + k_{cush_V}}{2 \cdot m_W} & -\frac{b_R + b_{cush_V}}{2 \cdot m_W} & \frac{k_{cush_V}}{2 \cdot m_W} & \frac{b_{cush_V}}{2 \cdot m_W} \\ 0 & 0 & 0 & 1 \\ \frac{k_{cush_V}}{m_B} & \frac{b_{cush_V}}{m_B} & -\frac{k_{cush_V}}{m_B} & -\frac{b_{cush_V}}{m_B} \end{bmatrix}, \qquad \underline{B} = \begin{bmatrix} 0 \\ 1 \\ 0 \\ 1 \end{bmatrix},$$

$$\underline{C} = \begin{bmatrix} 1 & 0 & 0 & 0 \\ 0 & 1 & 0 & 0 \\ 0 & 0 & 1 & 0 \\ 0 & 0 & 0 & 1 \end{bmatrix}, \qquad \underline{D} = \begin{bmatrix} 0 \\ 0 \\ 0 \\ 0 \end{bmatrix},$$

and for the rotated drop:

$$\underline{x} = \begin{bmatrix} x_1 \\ x_2 \\ x_3 \\ x_4 \\ x_5 \\ x_6 \end{bmatrix},$$

$$\underline{u} = [g],$$

$$\underline{A} = \begin{bmatrix} 0 & 1 & 0 & 0 & 0 & 0 \\ -\frac{k_R + k_{cush_H}}{m_W} & -\frac{b_R + b_{cush_H}}{m_W} & \frac{k_{cush_H}}{m_W} & \frac{b_{cush_H}}{m_W} & 0 & 0 \\ 0 & 0 & 0 & 1 & 0 & 0 \\ \frac{k_{cush_H}}{m_B} & \frac{b_{cush_H}}{m_B} & -\frac{2k_{cush_H}}{m_B} & -\frac{2b_{cush_H}}{m_B} & \frac{k_{cush_H}}{m_B} & \frac{b_{cush_H}}{m_B} \\ 0 & 0 & 0 & 0 & 0 & 1 \\ 0 & 0 & \frac{k_{cush_H}}{m_W} & \frac{b_{cush_H}}{m_W} & -\frac{k_{cush_H}}{m_W} & -\frac{b_{cush_H}}{m_W} \end{bmatrix}, \quad \underline{B} = \begin{bmatrix} 0 \\ 1 \\ 0 \\ 1 \\ 0 \\ 1 \end{bmatrix},$$

$$\underline{C} = \begin{bmatrix} 1 & 0 & 0 & 0 & 0 & 0 \\ 0 & 1 & 0 & 0 & 0 & 0 \\ 0 & 0 & 1 & 0 & 0 & 0 \\ 0 & 0 & 0 & 1 & 0 & 0 \\ 0 & 0 & 0 & 0 & 1 & 0 \\ 0 & 0 & 0 & 0 & 0 & 1 \end{bmatrix}, \quad \underline{D} = \begin{bmatrix} 0 \\ 0 \\ 0 \\ 0 \\ 0 \\ 0 \end{bmatrix}.$$

Note that the forcing input $\underline{u}$ merely represents the gravitational force acting on the bodies.

To obtain as output the displacement and velocity of each mass in the system, we set:

$$\underline{w} = \underline{x}$$

for both models.

3.7.2 - Impact Forces

It is not the *net* force on the masses that are of interest, but rather the forces resulting in compressive stress on the components. For example, consider a mass with a 4 N force applied from above and a 6 N force applied from below. The net force is 2 N upward, causing an upward acceleration of the mass. However, it is the equal and opposite components of the two forces causing compression, i.e. the smaller of the two forces (4 N).

For our model, we will denote the downward force applied from above as F_a and that applied from below as F_b. Note that for the upright analysis, we must revert to the form shown in Figure 23(a), as we are no longer interested in the net force only. It follows that the forces of interest on the wheel for the upright drop are, in matrix form:

$$F_{a_W} = \frac{1}{2}\begin{bmatrix} -k_{cush_V} & -b_{cush_V} & k_{cush_V} & b_{cush_V} \end{bmatrix} \cdot \underline{w} + m_W \cdot \underline{u}$$
$$F_{b_W} = \frac{1}{2}\begin{bmatrix} -k_R & -b_R & k_R & b_R \end{bmatrix} \cdot \underline{w}$$

In theory, under the assumption that the spring and damping constants above and below the wheel are equal, the maximum compressive force on the central body is simply its own weight. This is not the case for the rotated drop, where the wheel and body forces are:

$$F_{a_W} = \begin{bmatrix} -k_{cush_H} & -b_{cush_H} & k_{cush_H} & b_{cush_H} & 0 & 0 \end{bmatrix} \cdot \underline{w} + m_W \cdot \underline{u}$$
$$F_{b_W} = \begin{bmatrix} -k_R & -b_R & 0 & 0 & 0 & 0 \end{bmatrix} \cdot \underline{w}$$
$$F_{a_B} = \begin{bmatrix} 0 & 0 & -k_{cush_H} & -b_{cush_H} & k_{cush_H} & b_{cush_H} \end{bmatrix} \cdot \underline{w} + m_B \cdot \underline{u}$$
$$F_{b_B} = \begin{bmatrix} -k_{cush_H} & -b_{cush_H} & k_{cush_H} & b_{cush_H} & 0 & 0 \end{bmatrix} \cdot \underline{w}$$

Note that the all models are valid only for x1 = > 0 (while the wheel is in contact with the ground). This is not a problem, because the forces of interest are the maximum ones, which occur during the wheel-to-ground contact.

For all cases, the force acting to compress the mass is the minimum of F_a and F_b. When this force is a maximum, the greatest stress will be experienced by the mass. The above systems were used to perform simulations have been in *MATLAB*, and the maximum forces experienced by the wheel and central body were determined.

The impact analysis was performed using the gravitational acceleration of Earth, as this is the worst place for ATOM to drop. The maximum forces found are summarized in *Table 3*. Because of the large uncertainty associated with the model, other simpler tools were used to provide comparisons.

Component	Axial Force (N)	Radial Force (N)
Shell	31500	15100
Body	740	490

Table 3: Impact forces

A rule of thumb regarding impact forces was applied, which states that the impact force is equal to the weight multiplied by one plus the ratio of the stopping to falling distance (Huang, 2006). This calculation does not consider the spring/damper effects of the cushions, thus it should be on the high side.

A web-based applet was also used, which can be found at http://hyperphysics.phy-astr.gsu.edu/hbase/impcal.html#c1. This applet is very simple and thus is not reliable for determining design numbers. However, it gives a rough approximation and can be used to determine if the model results are in the right ballpark.

The rotated drop force on the wheel was used to compare the values, which was calculated to be 31500 N with *MATLAB* model. The rule of thumb gave an impact force of 46900 N (higher than the model force, as expected), and the applet gave a force of 14300 N. It is encouraging to see that all methods give results of the same order of magnitude.

3.7.3 - Impact Stresses

A finite element analysis was performed on the shell, considered to be the critical component due to its thin walls and high impact force exposure. To model the stress state, one end of the shell was fixed, and on the other end the maximum shell force found during the impact analysis was applied to the area in contact with the ground.

The result was a maximum stress of less than 13 MPa, which is below the yield stress of 24-34 MPa. In reality, the presence of the cushion will significantly spread the load, resulting in a lower stress. The safety factor for the Earth-based impact is thus greater than two.

Note that sufficient space is left in the central body to install an individual suspension system for more sensitive equipment, if required.

3.8 – Bearings

Thin section bearings were selected for the application due to their low mass, small space requirements, and large bore diameters. It is necessary that the bearings be sealed to prevent dust from getting through.

The bearings were chosen based on the maximum forces found during the impact analysis. It is the body forces in *Table 4* that the bearings must handle, i.e 740 N in the axial (thrust) direction, and 490 N in the radial. Because there is a large uncertainty regarding these forces (due to the unknown damping constants), a large safety factor was desired for the bearing loads. The sealed version of the JSA045 bearing from *Silverthin, Inc.*, was selected based on its dimensions. The dynamic thrust and radial loads permitted by *each* bearing are 5840 N and 2330 N, respectively.

4.0 - Budget

A preliminary budget, shown in *Table 4*, has been drawn based on the decisions made during the first phase of the design. The suppliers quoted are the ones who provided the prices below, but they are only suggestions (especially in the case of the battery). It is likely that better options exist and may be worthwhile to explore. Although specialized work costs were considered, basic labour costs were neglected under the assumption that the building phase will be performed as coursework at McGill University.

Note that values for the cost of the motors, transmission, solar panels, communication system, and CPU, which will be determined in the next phase of the design, are currently unknown. The total cost of these components was estimated as $5000, but this is an extremely wild guess.

Note that the budget does not include taxes or shipping costs. Prices quoted in US dollars have been converted to Canadian using the current exchange rate of $1 US = $1.15 CAN.

Part/Procedure	Cost	Supplier
Sensor	$1,595.00	Microstrain, Inc.
Wheel Shells	$236.00	Franjo Metal, Inc.
Rubber Layer	$1,618.00	Rematech, Inc.
Battery	$4,025.00	Lithion, Inc.
Foam Fill	$70	Smooth-On, Inc.
Raw Materials/Small Parts	$300.00	various
Solar Panels	$5,000.00	N/A
Motors		
Transmission		
Communications		
CPU		
TOTAL COST	$12,844.00	

Table 4: Budget

5.0 – Conclusions & Recommendations

The first phase of the ATOM design has been completed, with the main concepts and components selected. Tasks to be performed in future phases of the design are the following:

- Detailed design of the transmission system or equivalent mechanism (including motor choice)
- Detailed electrical load analysis and circuit design
- Computer programming
- Communication system selection
- Solar panel detail design
- Torsion hinge selection
- Dust protection for the hinges and cable holes
- Mission-specific equipment choice
- Consideration of an alternate suspension (see *Section 3.1.2*)

The torsion hinges connecting the array panels must also be selected. The requirements have been determined in the current work, so this should be a simple matter of finding appropriate commercial products for the job.

The complexity of adding a tilting mechanism (as originally conceptualized and depicted in *Figure 14*) was beyond the scope of this project, but it is recommended to develop in detail for future optimization. It is also recommended that a second opinion by someone with experience in the planetary navigation be obtained regarding the torque and power analysis of the motors.

It may be desirable to sacrifice a small amount of the solar array area to make space for external sensors or other instrumentation such as a camera. It should be noted, though, that ATOM exhibits a constant rocking motion while driving; it is thus unpractical to use for example, a camera while in this mode. Another option for the camera might be to locate the lense beneath the solar panels, requiring the panels to be deployed during its use. Since ATOM would need to be still for camera use in any case, this might not be such an inconvenience. Sensors could also be placed on the legside end cylinder between the end of the solar panels and the end cap (see *Figure 8*). It may be desirable to incorporate sensors to detect obstacles that may scrape the body of ATOM, and corresponding control to avoid them.

The exact layout of the components within the central body should not be determined until all the components are finalized.

Due to time constraints and lack of available tools/knowledge, simple models were used for the impact analysis. Care was taken to ensure that these models were all conservative, i.e. the assumptions made would lead to greater stresses. Safety factors are thus inherently present in the design; however, their magnitude is unknown and in many places may be quite large.

Stress analysis on every part was not possible due to time constraints. However, the parts that were considered "critical" (i.e. the most likely to yield under impact conditions) proved to be well below the yield stress of the materials.

It is recommended to perform a detailed stress analysis (impact and otherwise) to determine the maximum permissible impact, and potentially shave material where possible for the purposes of weight reduction.

Although specific manufacturing and assembly methods have been suggested for the non-trivial parts, it was not considered worthwhile to produce official manufacturing plans until the design is complete. Significant changes will likely be made in the second phase of the design, rendering such plans obsolete. Detailed drawings have been included for custom parts, found in *Appendix I*.

If, following success of the prototype, the design is used for actual Mars missions, a temperature regulation system would be desirable to ensure that all equipment is within its operating temperature range. In addition, if the choice of rubber is maintained for a Mars mission, a softer rubber maintaining its material properties at low temperatures such as silicone rubber should be used.

6.0 - References

Barnard R.H., Jefferson C.M. (2002) Hybrid Vehicle Propulsion. WIT Press, Southampton.

Boudreault E., Gosselin, C. (2006) Design of Sub-Centimetre Underactuated Compliant Grippers. In: Proceedings of IDETC/CIE

Brant B. (1994) Build Your Own Electric Vehicle. McGraw Hill Inc., New York.

Huang M. (2002) Vehicle Crash Mechanics. CRC Press LLC, Florida.

Boudreault E., Gosselin, C. (2006) Design of Sub-Centimetre Underactuated Compliant

Iagnemma K., Dubowski S. (2004) Mobile Robots in Rough Terrain. Springer Berlin Heidelberg ,New York

Kang S. (2003) Terrain Parameter Estimation and Traversability Assessment for Mobile Robots. M.S. Thesis, Massachusetts Institute of Technology

Krauter S. (2006) Solar Electric Power Generation. Springer Berlin Heidelberg, New York

Landis A., Appelbaum J. (1991) Photovoltaic Power Options for Mars. In: Space Power, Vol. 10, pp 225-237 (1991).

Nasrallah D.S. (2006) Modeling and Control of Two-Wheeled Mobile Robots on Uneven Terrain. Ph.D. Thesis, McGill University, Montreal

Ratnakumar B. V. , Smart M. C. (2006) An Update on the Performance of Li-Ion Rechargeable Batteries on Mars Rovers. Jet Propulsion Laboratory, California Institute of Technology

Wong, J.Y. (2001) Theory of Ground Vehicles. John Wiley & Sons Inc., New York.